



Near-wall turbulence of a vertical buoyancy-driven boundary layer

Krishna Reddy Maryada ¹, Steven W. Armfield ², Michael MacDonald ¹, Priyanka Dhopade ¹ and Stuart E. Norris ¹

Corresponding author: Krishna Reddy Maryada, krishna.reddy.maryada@auckland.ac.nz

(Received 20 February 2025; revised 8 August 2025; accepted 18 September 2025)

Using direct numerical simulations, we systematically investigate the inner-layer turbulence of a turbulent vertical buoyancy layer (a model for a vertical natural convection boundary layer) at a constant Prandtl number of 0.71. Near-wall streaky structures of streamwise velocity fluctuations, synonymous with the buffer layer streaks of canonical wall turbulence, are not evident at low and moderate Reynolds numbers (Re) but manifest at high Re. At low Re, the turbulent production in the near-wall region is negligible; however, this increases with increasing Re. By using domains truncated in the streamwise, spanwise and wall-normal directions, we demonstrate that the turbulence production in the near-wall region at moderate and high Re is largely independent of large-scale motions and outer-layer turbulence. On a fundamental level, the near-wall turbulence production is autonomous and self-sustaining, and a well-developed bulk is not needed to drive the inner-layer turbulence. Near-wall streaks are also not essential for this autonomous process. The type of thermal boundary condition only marginally influences the velocity fluctuations, revealing that the turbulence dynamics are primarily governed by the meanshear induced by the buoyancy field and not by the thermal fluctuations, despite the current flow being solely driven by buoyancy. In the inner layer, the spanwise wavelength of the eddies responsible for positive shear production is remarkably similar to that of canonical wall turbulence at moderate and high Re (irrespective of near-wall streaks). Based on these findings, we propose a mechanistic model that unifies the near-wall shear production of vertical buoyancy layers and canonical wall turbulence.

Key words: turbulent convection, turbulent boundary layers, buoyant boundary layers

¹Department of Mechanical and Mechatronics Engineering, The University of Auckland, Auckland 1010, New Zealand

²School of Aerospace, Mechanical and Mechatronic Engineering, The University of Sydney, New South Wales 2006, Australia

1. Introduction

Buoyancy-driven boundary layer flow next to a vertical heated surface is central to many natural and industrial flows (Fan *et al.* 2021). For example, concerning industrial flows, where the Reynolds/Grashof numbers are low-to-moderate, these are applicable for modelling room ventilation systems and free convection cooling of mechanical and electrical components (Bejan 2013). On geophysical scales, where the Reynolds/Grashof numbers are large, these are relevant to understanding anabatic flows over steep cliffs and melting of ice sheets (Wells & Worster 2008; McConnochie & Kerr 2016; Giometto *et al.* 2017; Howland *et al.* 2022).

The ambient is often (weakly) stably stratified in most real-world situations, and natural convection boundary layers frequently develop over vertical surfaces under such conditions (Bejan 2013). The vertical buoyancy layer, based on Prandtl's one-dimensional solution for 'mountain-valley winds' (Prandtl 1952), is a model of a vertical natural convection boundary layer immersed in a stably stratified medium (Gill 1966), and it has been studied through the years to understand the dynamics of vertical convection in the presence of ambient stable stratification. The current study uses the same formulation to model a vertical buoyancy-driven boundary layer.

Most studies on vertical buoyancy layers focus on stability and transition (e.g. Gill & Davey 1969; Tao, Le Quéré & Xin 2004; McBain, Armfield & Desrayaud 2007; Maryada et al. 2022), with there being only a few studies investigating the turbulent structure. Fedorovich & Shapiro (2009) investigated the vertical buoyancy layer's mean flow and one-point turbulent statistics with a constant heat flux thermal boundary condition. The authors found that the turbulent mean flow profiles were qualitatively similar to the laminar flow. At the low-to-moderate Reynolds numbers investigated, most of the turbulence was observed in the outer layer, and no signs of significant inner-layer turbulent activity were reported. In both laminar and turbulent vertical convection (both with and without ambient stable stratification), the velocity maximum and its corresponding wall-normal location are often used in the theoretical analyses of the flow close to the heated wall (Lin & Armfield 2005; Ng et al. 2017; Ke et al. 2021; Howland et al. 2022) or to demarcate the different regions of the flow (Tsuji & Nagano 1988a; Lin, Armfield & Patterson 2008; Fedorovich & Shapiro 2009; Ke et al. 2023). In terms of demarcation, the region between the heated wall and the velocity maximum is often defined as the inner layer, inner flow region or nearwall region. The region beyond the velocity maximum is defined as the outer layer, outer side or outer bulk region. In this study, we also use the velocity maximum to demarcate the different flow regions. The 'outer layer' is defined as the wall-normal region beyond the velocity maximum, while the 'inner layer' is defined as the wall-normal region between the heated wall and the velocity maximum. Note that this is different to the traditional inner and outer layer definitions commonly employed in canonical wall turbulence, and any mention of the inner and outer layers in this paper corresponds to the above definitions.

As an extension to the study of Fedorovich & Shapiro (2009), Giometto *et al.* (2017) investigated the turbulent structure of vertical buoyancy layers using a constant temperature excess boundary condition and found that the two flows are qualitatively similar in the outer layer. Giometto *et al.* (2017) also investigated the inner-layer turbulence by examining the one-point turbulent kinetic energy (TKE) budget equation and proposed a four-layer structure, with the inner layer featuring a laminar-like sublayer and a buffer layer where nonlinear TKE transport terms mostly balance dissipation and viscous diffusion. Using two-point correlations and energy spectra, it was also shown that the outer layer of the vertical buoyancy layer is populated with streamwise-elongated large-scale motions (LSMs) of streamwise velocity fluctuations, carrying significant amounts of TKE and Reynolds shear stress (Schumann 1990; Maryada *et al.* 2023).

Vertical natural convection boundary layers immersed in stably stratified environments, such as the buoyancy layer, share many similarities with their unstratified counterparts (Bejan 2013). Significant progress has been made on this front in the past few decades when compared with its stratified counterparts; hence, it is briefly reviewed here.

Unstratified turbulent natural convection boundary layers over vertically heated surfaces were investigated using theoretical analyses, numerical simulations and experiments for well over 50 years. The experimental studies in the twentieth century (e.g. Vliet & Liu 1969; Cheesewright & Doan 1978; Miyamoto & Okayama 1982; Tsuji & Nagano 1988a, b) demonstrated that the turbulence development in vertical natural convection boundary layers is drastically different from turbulent boundary layers (canonical wall turbulence). These studies revealed that turbulent activity is primarily dominant in the outer layer. Direct numerical simulations (DNSs) (Abedin, Tsuji & Hattori 2009; Gayen, Griffiths & Kerr 2016; Howland et al. 2022) and experiments (McConnochie & Kerr 2016; Parker et al. 2021; Nakao et al. 2023) of vertical convection at different Prandtl numbers in the subsequent years confirmed the observations regarding the turbulence activity in the outer layer. This behaviour is qualitatively similar to the turbulent vertical buoyancy layer, at least at the Reynolds numbers investigated in prior studies (Fedorovich & Shapiro 2009; Giometto et al. 2017; Maryada et al. 2023).

However, turbulence is not always limited to the outer layer of vertical natural convection boundary layers. It was theorised by Wells & Worster (2008) that vertical natural convection boundary layers first undergo a laminar–turbulent transition to a turbulent state where most of the turbulence is dominant in the outer layer (also see Kraichnan (1962) and Grossmann–Lohse theory of Rayleigh–Bénard convection (Grossmann & Lohse 2000)). At higher Reynolds/Grashof numbers, such as those relevant to geophysical scales, the vertical natural convection boundary layer undergoes a second transition, where the inner layer becomes turbulent in the sense of Prandtl and von Kármán. In this regime, appreciable turbulent activity is present in the inner and outer layers, with the inner layer exhibiting signatures of canonical wall turbulence, i.e. near-wall streaks (Kline *et al.* 1967; Hutchins & Marusic 2007; Hwang, Lee & Sung 2020). Following the terminology of the Grossmann–Lohse theory from hereon, the first turbulent regime is termed the 'classical regime', and the second turbulent regime is termed the 'ultimate regime'.

The DNS results of Ng *et al.* (2017) and Ke *et al.* (2023) have provided compelling evidence of such a transition. At low-to-moderate Reynolds/Grashof numbers, most of the turbulence is observed in the outer layer, with the inner layer being weakly turbulent. The inner layer of a buoyancy-driven vertical boundary layer becomes turbulent in the sense of Prandtl and von Kármán at sufficiently high Reynolds/Grashof numbers. It was demonstrated that at sufficiently high Grashof numbers, the inner layer is characterised by peaks in the streamwise and spanwise energy spectra of streamwise energy fluctuations, whose wavelengths are comparable to the near-wall streaks observed in canonical wall turbulence.

Despite the promising results of Ng et al. (2017) and Ke et al. (2023), our understanding of turbulence in the inner layer of vertical convection is far from complete, with there even being contradictory views on the turbulence dynamics that are central to governing buoyancy-driven boundary layers.

For example, Tsuji & Nagano (1988b) and Hattori et al. (2006) suggest that the Reynolds shear stress in the inner layer is almost zero. However, the experimental results of Miyamoto & Okayama (1982), and the numerical simulations of Fedorovich & Shapiro (2009), Kiš & Herwig (2012), Giometto et al. (2017), Sebilleau et al. (2018), Ke et al. (2020, 2023) and Maryada et al. (2023) contend that in vertical convection, the Reynolds shear stress in the near-wall region can be negative both in isothermal and stably

stratified environments. The lack of consensus also extends to the streamwise buoyancy flux, responsible for TKE production in vertical convection (To & Humphrey 1986). In unstratified vertical convection, Miyamoto & Okayama (1982) argue that it is negative in the inner layer; however, Tsuji & Nagano (1988b) argue the contrary. Giometto *et al.* (2017) and Maryada *et al.* (2023) only report positive values of buoyancy flux in the inner layer of vertical buoyancy layers. The results of Ke *et al.* (2023) suggest that the behaviour of the mean buoyancy flux in the near-wall region is a function of *Re*, with its magnitude increasing with increasing Reynolds number. Ke *et al.* (2023) report negative values of streamwise turbulent heat flux.

Even regarding the inner layer turbulence in general, it has been suggested that the outer bulk can drive the inner layer and contributes significantly towards the inner-layer turbulence sustenance in the ultimate regime (Wells & Worster 2008; Ng *et al.* 2017). However, to date, there is no conclusive evidence in support of or against this hypothesis.

It is evident from the above discussion that the near-wall region of vertical natural convection boundary layers, let alone vertical buoyancy layers, has not been investigated thoroughly, with there still being several unanswered questions relating to the dynamics of near-wall turbulence. Here, using DNSs, we systematically investigate the following aspects of inner-layer turbulence of vertical buoyancy layers in both the classical and ultimate regimes.

The first objective of the current study is to understand the fundamental processes governing the inner-layer turbulence of vertical buoyancy layers at low, moderate and high Reynolds numbers. Specifically, we examine whether the inner-layer turbulence is self-sustaining and autonomous, and whether the bulk flow and LSMs are essential for the inner-layer to become turbulent in the sense of Prandtl and von Kármán. In vertical convection, the TKE is produced due to both shear and buoyancy. Hence, intuitively, one would expect the type of thermal boundary condition (prescribed temperature (Dirichlet boundary condition) versus prescribed heat flux (Neumann boundary condition)) to be significant in determining the dynamics of the inner-layer turbulence. This has not been addressed thoroughly in the past and is the second objective of this study. Understanding these aspects would aid in developing reduced-order and turbulence models for vertical natural convection flows, which currently lag behind the turbulence models of canonical wall turbulence.

The paper is organised as follows. The mathematical notation, governing equations and computational methods are introduced in § 2. The inner-layer turbulence of the vertical buoyancy layer at low and moderate Reynolds numbers is investigated in §§ 3.1 and 3.2, where the key aspects relating to the conundrum of Reynolds shear stress and streamwise turbulent heat flux in the inner layer are addressed. In §§ 3.3 and 3.4, it is demonstrated that at moderate and high *Re*, the inner-layer turbulence can be sustained even if the LSMs that populate the outer layer or bulk flow are not represented accurately. The effect of thermal boundary conditions is also examined in §§ 3.2 and 3.4. A mechanistic model of turbulence sustenance in the inner layer at moderate and high Reynolds numbers is presented in § 3.5. The conclusions are given in § 4.

2. Governing equations and numerical methodology

Let us consider a linearly heated vertical wall placed in a stably stratified ambient medium (having a positive vertical temperature gradient γ_s). The heated wall has a temperature T_w , and the ambient medium has a temperature T_∞ . Both temperatures increase linearly with height (in the positive x_2 direction as we define the wall-normal, streamwise and spanwise using x_1 , x_2 and x_3 , respectively) such that there is always a constant temperature

difference between the heated wall and the ambient medium ($\Delta T = T_w(x_2) - T_\infty(x_2) = B$). In such cases, an equilibrium natural convection boundary layer with a constant boundary layer thickness develops over the heated surface. This boundary layer is termed the buoyancy layer (Prandtl 1952; Gill 1966), and we use it to model a natural convection boundary layer immersed in a stably stratified medium.

The following non-dimensional Navier–Stokes equations with the Oberbeck–Boussinesq approximation for buoyancy and the scalar transport equation are solved to model the flow:

$$\frac{\partial \tilde{u}_i}{\partial x_i} = 0, (2.1a)$$

$$\frac{\partial \tilde{u}_i}{\partial t} + \tilde{u}_j \frac{\partial \tilde{u}_i}{\partial x_j} = -\frac{\partial \tilde{p}}{\partial x_i} + \frac{1}{Re} \frac{\partial^2 \tilde{u}_i}{\partial x_j^2} + \frac{2}{Re} \tilde{\vartheta} \delta_{i2}, \tag{2.1b}$$

$$\frac{\partial \tilde{\vartheta}}{\partial t} + \tilde{u}_j \frac{\partial \tilde{\vartheta}}{\partial x_j} = \frac{1}{RePr} \frac{\partial^2 \tilde{\vartheta}}{\partial x_j^2} - \frac{2}{RePr} \tilde{u}_2, \tag{2.1c}$$

where $Re = U_{\Delta T} \delta_l / \nu = (\mathbf{g} \beta \Delta T \delta_l^3) / 2\nu^2$ is the Reynolds number, and $Pr = \nu / \alpha$ is the Prandtl number. Here, $\delta_l = (4\nu\alpha/\mathbf{g}\beta\gamma_s)^{1/4}$ and $U_{\Delta T} = \Delta T (\mathbf{g}\beta\alpha/\nu\gamma_s)^{1/2}$ are characteristic length and velocity scales, ν is the kinematic viscosity, α is the thermal diffusivity, β is the coefficient of thermal expansion and \mathbf{g} is the acceleration due to gravity. The Grashof number is twice the Reynolds number, and the Prandtl number is 0.71. The non-dimensionalisation is the same as in Gill & Davey (1969) and Maryada et al. (2022).

The instantaneous non-dimensional velocity field is represented using \tilde{u}_i , \tilde{p} is the instantaneous pressure field and $\tilde{\vartheta}$ is the instantaneous non-dimensional temperature field, also called the buoyancy field. The buoyancy field is defined as the temperature excess over the ambient scaled by ΔT , defined as $\tilde{\vartheta} = (T - T_{\infty})/\Delta T$.

A geometric representation of the computational domain and coordinate system, and a schematic of the vertical buoyancy layer in the relevant non-dimensional variables are shown in figures 1(a) and 1(b). Near the edge of the boundary layer, there is a flow reversal and a region of $\tilde{\vartheta}$ deficit, which are notably absent in temporally evolving vertical natural convection boundary layers immersed in isothermal media (cf. figure 1 in Ke *et al.* 2020). Nevertheless, the mean flow behaviour near the heated wall (within δ_i) is qualitatively similar to unstratified vertical natural convection and is the region of interest in the current study.

An in-house collocated finite volume code (Norris 2000; Armfield *et al.* 2003) that is second-order accurate spatially and temporally was used to perform DNSs. The code has been extensively verified and validated in the past on several natural convection flows (Armfield *et al.* 2003; Maryada *et al.* 2022). A second-order centre difference scheme was used for spatial discretisation. The diffusion and advection terms were integrated in time using a second-order accurate Crank–Nicolson scheme and a second-order Adams–Bashforth scheme, respectively. The Courant number was always less than 0.4. In non-staggered finite volume numerical solvers, simple linear interpolation of the cell-centre velocities to get the cell-face velocities would lead to checkerboarding of the pressure field (Patankar 1980). To alleviate this issue, the in-house code uses the Rhie–Chow interpolation for velocity (Rhie & Chow 1983), as it is well known that Rhie–Chow interpolation or similar schemes retain the grid-scale ellipticity, thereby avoiding spurious oscillations in the pressure field (Armfield 1991, 1994). The divergence of the velocity field

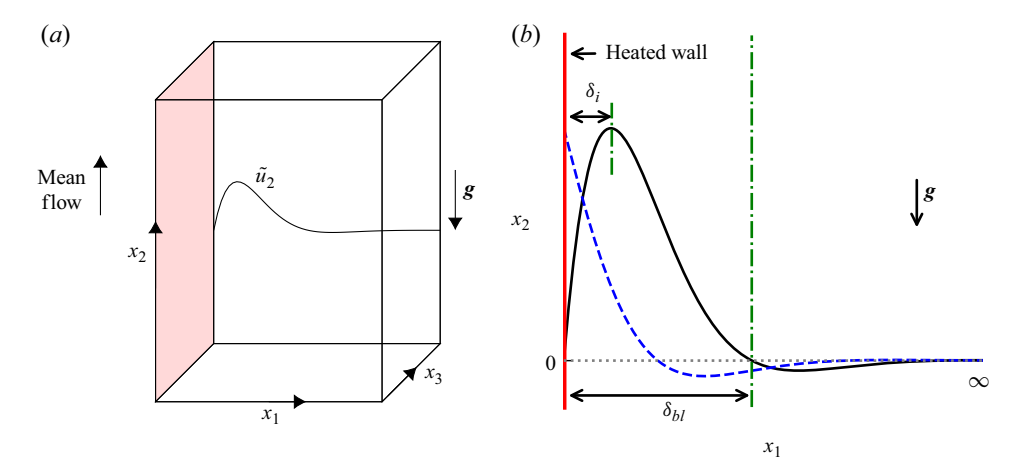


Figure 1. A schematic of the flow configuration (not to scale). Panel (a) is a schematic of the computational domain and the coordinate system, with the shaded red region representing the heated wall. Panel (b) shows streamwise velocity and temperature fields in the relevant non-dimensional variables. Here, the black solid curve is the streamwise velocity \tilde{u}_2 , and the blue dashed curve is the buoyancy field, the non-dimensional temperature field $\tilde{\vartheta}$. The inner layer width is given by δ_l , and the boundary layer thickness is given by δ_{bl} .

was also checked after every time step, and it was always below 5×10^{-10} . The reader is referred to Maryada *et al.* (2023) for further details on the numerical methods.

The mean streamwise velocity and buoyancy fields are represented using $\overline{u_2}$ and $\overline{\vartheta}$, respectively. The mean scalar and vector fields are calculated by averaging the instantaneous fields in time and in the homogeneous spatial (streamwise and spanwise) directions The fluctuations are represented using u_i and ϑ such that $\widetilde{u}_i = \overline{u_i} + u_i$ and $\widetilde{\vartheta} = \overline{\vartheta} + \vartheta$. The ensemble-averaged (averaged in time and the homogeneous spatial directions) one-point turbulence quantities are represented using $\langle \cdot \rangle$. The variables with the superscript + indicate that these are normalised using viscous units, i.e. friction velocity $(u_\tau = \sqrt{\tau_w/\rho})$, friction temperature $(\theta_\tau = q_w/(\rho C_p u_\tau))$ and kinematic viscosity. Here, ρ is the density of the fluid, τ_w is the wall shear stress, q_w is the wall heat flux and C_p is the specific heat capacity of the fluid.

Fourteen DNSs with different parameter combinations (different domain sizes, *Re* and thermal boundary conditions) were performed to examine the turbulence in the inner layer of a vertical buoyancy layer. Due to the large parameter space, we introduce the following notation to describe the different simulation cases concisely. Throughout this paper, each case is represented using a combination of three letters that are followed by three/four numbers, e.g. 'ABCXXXX'. The first letter (letter 'A' in the example) represents the size of the domain in the wall-normal direction, with F representing full/regular domain size, R and R₂ representing reduced domain sizes. The second letter (letter 'B' in the example) indicates the size of the domain in the streamwise (vertical) and spanwise directions, with F representing the full/regular domain size, and S and L representing reduced domain sizes in the streamwise (vertical) and spanwise directions. The third letter (letter 'C' in the example) represents the thermal boundary condition, with D indicating a constant temperature excess boundary condition (Dirichlet boundary condition) and N representing a constant heat flux boundary condition (Neumann boundary condition). The last three/four digits ('XXXX' in the example) indicate *Re*.

In the wall-normal direction, a domain is considered to be full if the wall-normal extent of the domain is sufficiently large to not influence the boundary layer flow. A domain

is termed reduced if the wall-normal extent of the computational domain significantly affects the boundary layer flow. Regarding reduced wall-normal domains, cases with R₂ as the first letter have smaller wall-normal domain sizes than those with R as the first letter. In the streamwise (vertical) and spanwise directions, a domain is termed full if the two-point correlations of the most energetic structures decay to zero in the streamwise and spanwise directions. The letters S and L are used to represent domains that do not satisfy these criteria. Cases with S as the second letter have streamwise and spanwise domain sizes smaller than those with L as the second letter. The relevant details of the simulations are elaborated in the respective sections of the paper for continuity.

3. Results and discussion

As discussed in § 1, turbulent vertical natural convection boundary layers can be separated into two regimes (Wells & Worster 2008; Ng et al. 2017; Ke et al. 2023). First is the classical regime, which is relevant at low and moderate Reynolds numbers. Here, most of the turbulence is observed in the outer layer, with the inner layer being weakly turbulent. At sufficiently high Reynolds numbers, the natural convection boundary layer transitions to the ultimate regime, where the inner layer exhibits signatures of canonical wall turbulence. One of those signatures is the emergence of near-wall streaks, quantified by an energetic peak at a wavelength of $\lambda_{x_3}^+ \approx 100$ and a wall-normal distance of $x_1^+ \approx 15$ in one-dimensional energy spectra of streamwise velocity fluctuations in the spanwise direction.

Following Ng *et al.* (2017) and Ke *et al.* (2023), we differentiate between the classical and ultimate regimes using the one-dimensional energy spectra of streamwise velocity fluctuations in the spanwise direction. The presence of a spectral peak at $\lambda_{x_3}^+ \approx 100$ and $x_1^+ \approx 15$ is considered as a signature of the ultimate regime, while its absence implies that the vertical natural convection boundary layer is still in the classical regime.

3.1. Near-wall turbulence at low and moderate Reynolds numbers

First, we investigate the inner-layer turbulence (turbulence across δ_i in figure 1b) at low and moderate Re. To this end, we have performed numerical simulations at $200 \le Re \le 2800$ in large domains. The details of the domain and mesh are shown in table 1. Here, the domain sizes in the streamwise/vertical (x_2) and spanwise (x_3) directions are comparable to the domain sizes of Giometto et al. (2017). The domain sizes in the streamwise and spanwise directions were also verified using two-point correlations and were found to be adequate (Moin & Kim 1982). The domain sizes employed in the wall-normal (x_1) direction are greater than the ones often used in the numerical simulations of boundary layer flows (Kozul, Chung & Monty 2016; Ke et al. 2020). Periodic boundary conditions were used in the streamwise and spanwise directions, as the flow is homogeneous in those directions. In the wall-normal direction, a no-slip velocity boundary condition ($\tilde{u}_i = 0$) for velocity was used at the heated wall (the thermal boundary condition is discussed below). Akin to prior studies on natural convection boundary layers (cf. Zhao, Lei & Patterson 2017; Maryada et al. 2022, 2023), an open-type boundary condition with $\tilde{\vartheta} = 0$ was used at the boundary opposite the heated wall. At the open-type boundary, the flow is allowed to enter and exit the domain freely. It was verified that there was no artificial pile-up of TKE or temperature variance at this boundary, and therefore, this boundary condition does not adversely affect the flow dynamics investigated in the present study.

In table 1, all case names begin with FF, indicating that these are full/regular domains in the wall-normal, streamwise (vertical) and spanwise directions. We classify a domain size

Case	Re	\approx Re $_{ au}$	Domain size $(x_1 \times x_2 \times x_3)$	$N_{x_1} \times N_{x_2} \times N_{x_3}$	Δx_{1w}^+	$\Delta x_{1\delta_{bl}}^+$	$\Delta x_2^+ \times \Delta x_3^+$
FFD200	200	80	$9.0\delta_{bl} \times 12.0\delta_{bl} \times 12.0\delta_{bl}$	$200 \times 182 \times 182$	0.46	1.6	4.7×4.7
FFD800	800	280	$6.8\delta_{bl} \times 25.1\delta_{bl} \times 9.4\delta_{bl}$	$350 \times 1400 \times 550$	0.42	3.3	4.9×4.9
FFD1400	1400	460	$7.0\delta_{bl} \times 9.7\delta_{bl} \times 9.0\delta_{bl}$	$355 \times 906 \times 816$	0.42	6.3	4.8×4.8
FFD1800	1800	580	$6.5\delta_{bl} \times 8.5\delta_{bl} \times 8.1\delta_{bl}$	$390\times1028\times978$	0.40	7.4	4.8×4.8
FFN2800	2800	510	$6.8\delta_{bl} \times 9.0\delta_{bl} \times 8.5\delta_{bl}$	$390 \times 1028 \times 978$	0.37	6.6	4.5×4.5

Table 1. Simulation settings of DNS reported in this paper. Here, the domain size is normalised using the boundary layer thickness, while the grid sizes are normalised using the viscous length scale. The wall-normal cell size next to the heated wall is represented using Δx_{1w}^+ while the wall-normal cell size at the edge of the boundary layer is represented using Δx_{1bw}^+ . See the text for the notation used for case names.

as full/regular if its dimensions are comparable to the dimensions outlined in table 1, as these are sufficiently big to not adversely affect the statistical signature of LSMs. Moreover, these act as our reference simulations in the subsequent sections. Note that the FFD800 and FFD1800 DNS datasets were previously used in Maryada *et al.* (2023) and Maryada *et al.* (2024), respectively.

The laminar vertical buoyancy layer (Pr=0.71) with a constant non-dimensional temperature excess boundary condition bifurcates into a periodic state at Re=102.17 (Maryada *et al.* 2022). At Re=200, the flow transitions into a turbulent state, but low-Re=1000 effects are significant. The case FFD200 is specifically used to investigate the inner-layer turbulence at low Re_{τ} . Cases FFD800, FFD1400 and FFD1800 correspond to moderate Reynolds numbers. In terms of mean quantities, FFD800, FFD1400 and FFD1800 are largely similar with an Re_{τ} -dependence. Differences are only observed regarding mean buoyant production/destruction of TKE between FFD1800 and the former two, which are discussed in § 3.2.

For cases where the third letter is D, a constant non-dimensional temperature $\tilde{\vartheta}=1$ was used as the thermal boundary condition at the heated wall, corresponding to a Dirichlet thermal boundary condition. These are collectively called constant temperature excess simulations.

Note that in the case of a laminar flow, the solution of Prandtl (1952) and Gill (1966) is valid even if the linearly heated wall (Dirichlet thermal boundary condition) is replaced with a uniform heat flux (Neumann thermal boundary condition) at the heated wall (Shapiro & Fedorovich 2004). Despite the similarity of laminar flow, it is well known that the type of thermal boundary condition affects the linear stability of buoyancy layers. The laminar vertical buoyancy layer bifurcates into a periodic state at a lower critical Reynolds number in the presence of a Neumann thermal boundary condition when compared with a Dirichlet thermal boundary condition (McBain et al. 2007). Regarding turbulence, it is usually argued that approximate statistical equivalence exists between the Dirichlet and Neumann thermal boundary conditions in vertical convection (Parker et al. 2021). However, to the best of the authors' knowledge, the influence of thermal boundary conditions on the near-wall turbulence structure and dynamics of such flows is yet to be scrutinised in detail. Therefore, a simulation was also performed with a constant wallnormal temperature gradient boundary condition $\partial \vartheta / \partial x_1 = 1$ at the heated wall, which is a Neumann boundary condition. This is represented using FFN2800 in table 1 and referred to as a constant heat flux simulation from hereon. The friction Reynolds number of FFN2800 is comparable to FFD1400 and FFD1800.

All the simulations were run for at least five buoyancy periods, $T_{SB} = \pi Re \sqrt{Pr}$ (the time period based on the Brunt–Väisäla frequency in the current non-dimensional units (Gill &

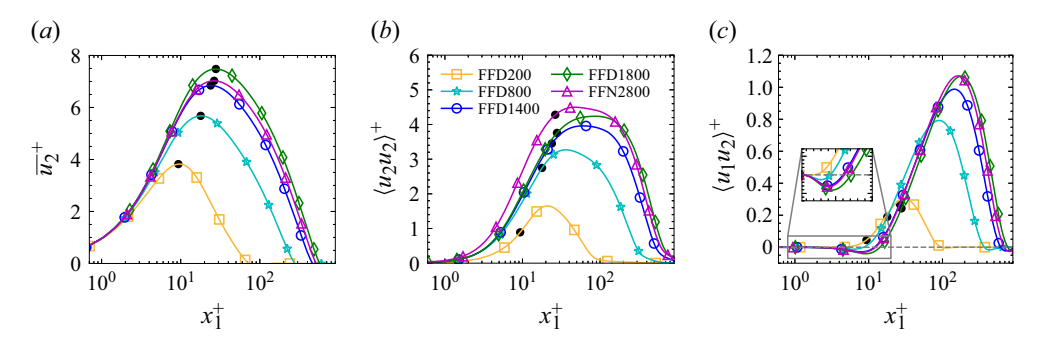


Figure 2. Profiles of (a) mean streamwise velocity $\overline{u_2}^+$, (b) mean streamwise velocity variance $\langle u_2 u_2 \rangle^+$ and (c) mean Reynolds shear stress $\langle u_1 u_2 \rangle^+$ at different Reynolds numbers. The location of the velocity maximum is represented using a solid black circle, which demarcates the inner layer from the outer layer. The symbols and all the subsequent figures are used only to differentiate the different cases.

Davey 1969)), for the flow to develop, and the statistics were calculated by averaging for the following three buoyancy periods. The time period used for the averaging process is similar to the time period of Giometto *et al.* (2017).

In table 1, we include the friction Reynolds number Re_{τ} , which was calculated from the DNS *a posteriori*. As noted by Ke *et al.* (2023), Re_{τ} does not include the effects of buoyancy and may not always be appropriate to characterise turbulence in buoyancy-driven vertical boundary layers. Nevertheless, we include it as a measure to understand scale separation present in the flow as Re_{τ} can be considered as the ratio of the eddies having scales $O(\delta_{bl})$ to the eddies having scales $O(\nu/u_{\tau})$.

As the ambient medium is stably stratified in the present case, it is vital to understand the role of stable stratification in the flow dynamics. The gradient Richardson number $Ri_g = (T_S/T_{SB})^2$ was calculated across the entire boundary layer thickness to determine the effect of stable stratification on the turbulence dynamics. Here, $T_S = |\partial \overline{u_2}/\partial x_1|$ is the shear time period and T_{SB} is the buoyancy time period as defined above. A value less than unity indicates that shear dominates over stratification, while a value greater than unity implies that stratification is significant (Tennekes & Lumley 1972).

For comparison, in an unstratified natural convection boundary layer, $Ri_g = 0$ as $T_{SB} = \infty$. In the case of the vertical buoyancy layer, at all the Re investigated, $Ri_g \ll 1$ in the inner layer, suggesting weak ambient stable stratification, and it is not a leading-order term. Therefore, we can safely ignore the effect of stable stratification on the turbulence dynamics, at least in terms of first- and second-order statistics considered in this study. Here, we emphasise that the shear observed in unstratified and stratified natural convection boundary layers is only due to the buoyancy force arising from a temperature difference between the heated wall and the ambient, not external forces. The current flow is not related to forced or mixed convection.

The mean streamwise velocity, streamwise velocity variance and the Reynolds shear stress are visualised in figure 2 to understand the general flow behaviour. The mean streamwise velocity field and the streamwise velocity variance are qualitatively similar to unstratified vertical natural convection boundary layers in the classical regime. The mean velocity field (shown in figure 2a) is zero at the heated wall due to a no-slip velocity boundary condition, increases and reaches a peak value before decreasing to zero as one approaches the edge of the boundary layer. Note that we define the boundary layer thickness δ_{bl} as the wall-normal location where the mean streamwise velocity changes sign for the first time (Maryada *et al.* 2023). The location of the velocity maximum demarcates

K.R. Maryada, S.W. Armfield, M. MacDonald, P. Dhopade and S.E. Norris

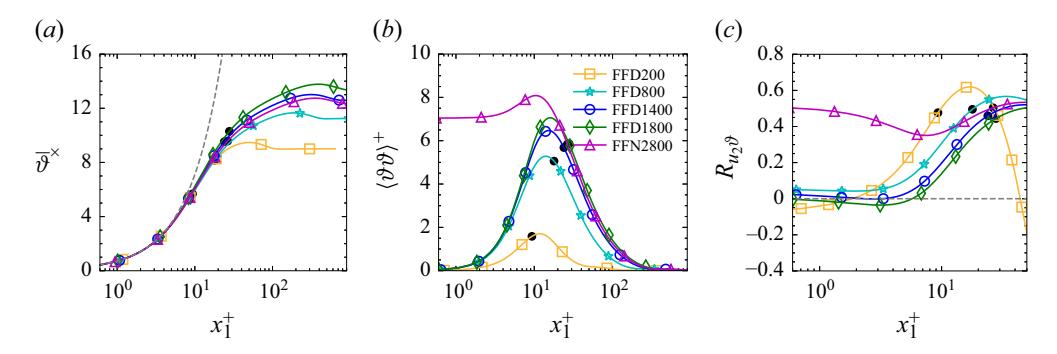


Figure 3. Profiles of (a) mean non-dimensional temperature field $\overline{\vartheta}^{\times}$, (b) mean buoyancy variance $(\vartheta \vartheta)^+$ and (c) one-dimensional correlation coefficient $R_{u_2\vartheta}$ at different Reynolds numbers. In panel (a), the grey dashed line represents $\overline{\vartheta}^{\times} = Prx_1^+$. Note that the horizontal scale in panel (c) is different from panels (a) and (b). The location of the velocity maximum is represented using a solid black circle, which demarcates the inner layer from the outer layer.

the inner layer from the outer layer, and the inner-layer width δ_i , when normalised in viscous units, is a function of Re_{τ} .

From the streamwise velocity variance in figure 2(b), it is apparent that the velocity variance peaks in the outer layer at all the Reynolds numbers investigated. A plateau or a peak is not observed in the inner layer, indicating that at these Reynolds numbers, the vertical buoyancy layer is not turbulent in the sense of Prandtl and von Kármán (Ke *et al.* 2023), i.e. the flow is not in the ultimate regime. The peak is a function of the friction Reynolds number and the thermal boundary condition.

The Reynolds shear stress is shown in figure 2(c), and as demonstrated in numerous prior numerical and experimental investigations of vertical convection (e.g. Tsuji & Nagano 1988a, b; Parker et al. 2021; Ke et al. 2023; Maryada et al. 2023), it peaks in the outer layer. However, significant differences are observed in the near-wall region. At Re = 200, the Reynolds shear stress is marginally positive (almost equal to zero) in the inner layer; however, at $Re \ge 800$, $\langle u_1 u_2 \rangle^+$ is negative in the inner layer irrespective of the thermal boundary condition. Note that it is not negative throughout the inner layer but only in the near-wall region. It is positive at the edge of the inner layer, which is due to the countergradient motions (Giometto et al. 2017). Investigating the counter-gradient motions is outside the scope of the current study.

The above implies a change in the turbulence production mechanism with an increasing Reynolds number. Therefore, in vertical convection, the Reynolds shear stress can be negative in the inner layer at moderate Re and need not always decay to zero as argued by Tsuji & Nagano (1988b) and Hattori $et\ al.$ (2006). The magnitude and sign of $\langle u_1u_2\rangle^+$ is a function of Re.

As the current flow is solely driven by buoyancy, i.e. the temperature field is an active scalar, it is imperative to examine its statistical behaviour to understand turbulence better. The mean buoyancy field is shown in figure 3(a). In the figure, the mean buoyancy field is calculated as $\overline{\vartheta}^{\times} = (\overline{\vartheta}_w - \overline{\vartheta})/\theta_{\tau}$, where $\overline{\vartheta}_w$ is the mean temperature at the heated wall and θ_{τ} is the friction temperature (Ke *et al.* 2020). In this study, we are primarily interested in the near-wall region. In this region, ϑ^{\times} of the constant temperature excess and constant heat flux simulations scale similarly, following $\overline{\vartheta}^{\times} = Prx_1^+$ scaling, indicating that the mean temperature field is primarily governed by conduction (Ke *et al.* 2020).

The wall-normal variation of the inner-normalised buoyancy variance $\langle \vartheta \vartheta \rangle^+$ is shown in figure 3(b). The buoyancy variance peaks at $x_1^+ \lesssim 20$ irrespective of the thermal boundary conditions. The buoyancy variance decays to zero at the wall for the constant temperature excess simulations (cases with the prefix FFD). For the constant heat flux boundary condition (FFN2800), the buoyancy variance is a non-zero value at the heated wall and is comparable to the peak magnitude. The 'less restrictive' nature of the Neumann-type flux boundary condition (McBain *et al.* 2007) ensures that the temperature fluctuations penetrate deep into the inner layer and exhibit non-zero values at the heated wall.

A mismatch between the streamwise velocity and buoyancy variance is apparent when comparing figures 2(b) and 3(b). The streamwise velocity variance peaks in the outer layer, but the buoyancy variance is dominant in the inner layer. This suggests a weak correlation between the streamwise velocity and buoyancy fluctuations in the near-wall region, i.e. the eddies transport $\langle u_2 u_2 \rangle^+$ and $\langle \vartheta \vartheta \rangle^+$ differently. To verify this, we calculate the one-point correlation coefficient between the buoyancy and streamwise velocity fluctuations $R_{u_2\vartheta}$ (which is the normalised streamwise turbulent heat flux), shown in figure 3(c). This is calculated as

$$R_{u_2\vartheta} = \frac{\langle u_2\vartheta\rangle^+}{\sqrt{\langle u_2u_2\rangle^+}\sqrt{\langle \vartheta\vartheta\rangle^+}}.$$
 (3.1)

At Re = 200, the correlation coefficient is weak in the inner layer. It is negative at $x_1^+ \lesssim 2$ and positive at greater wall-normal distances. For FFD800 and FFD1400, the correlation coefficient is weakly positive or close to zero. The absence of a strong correlation was also observed in unstratified turbulent natural convection boundary layers (Tsuji & Nagano 1988b). However, for FFD1800, it is marginally negative, indicating the dominance of coherent turbulent structures that promote negative correlation over those that promote positive correlation. This is discussed in detail in § 3.2 in terms of turbulence production.

On the other hand, the correlation coefficient for the constant heat flux boundary condition (FFN2800) exhibits a different trend than the constant temperature excess boundary condition (cases with the prefix FFD). In this case, the correlation coefficient is positive and around 0.45 throughout the inner layer, suggesting a good level of similarity between streamwise velocity and buoyancy fluctuations.

Therefore, approximate statistical equivalence between vertical convection flows over Dirichlet and Neumann thermal boundary conditions can be considered valid when one is interested in mean streamwise and buoyancy fields, Reynolds shear stress and velocity variances. However, the same cannot be said for buoyancy variance or the streamwise turbulent heat flux, as these are distinctly different between the two thermal boundary conditions, especially in the near-wall region.

3.2. Turbulence production in the inner layer at low and moderate Reynolds numbers Before explicitly focusing on the turbulent production mechanisms in the inner layer, we investigate the premultiplied one-dimensional energy spectra of streamwise velocity fluctuations to understand the general distribution of the eddies in vertical buoyancy layers. The premultiplied one-dimensional spectrum for an arbitrary zero-mean fluctuating quantity φ is defined as

$$\langle \varphi \varphi \rangle = \int_0^\infty k_i \phi_{\varphi \varphi}(k_i) d(\log k_i) = \int_0^\infty \phi_{\varphi \varphi}(k_i) d(k_i),$$
 (3.2)

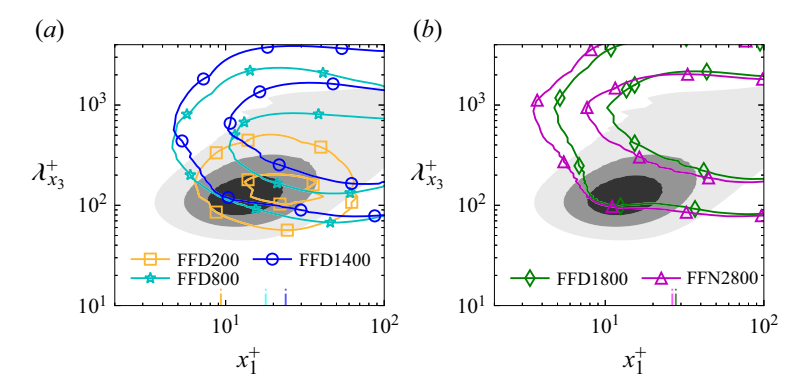


Figure 4. One-dimensional premultiplied energy spectra of streamwise velocity fluctuations in the spanwise direction at (a) Re = 200 (red squares), Re = 800 (cyan stars) and Re = 1400 (blue circles), and (b) Re = 1800 (green diamonds) and Re = 2800 (magenta triangles). Also shown is the one-dimensional premultiplied energy spectrum of streamwise velocity fluctuations in a turbulent channel flow at $Re_{\tau} \approx 1000$ (LM1000), which is from Lee & Moser (2015). The contour lines are 0.25 and 0.75 times the common maximum for the vertical buoyancy layer (1.06). The shaded contours correspond to 1, 2, 3 and 4 (light to dark) for LM1000. Vertical dash—dot lines near the abscissa indicate the edge of the inner layer. Symbols and colours for the vertical buoyancy layer are the same as in figure 2. The energy is normalised using viscous units.

where $\langle \varphi \varphi \rangle$ is the variance of φ , k_i is the wavenumber and $\phi_{\varphi \varphi}(k_i)$ is the spectrum. The term $k_i \phi_{\varphi \varphi}(k_i)$ is the one-dimensional premultiplied spectrum, such that the variance is equal to the area under the curve when plotted in a logarithmic scale. Consequently, peaks in the premultiplied spectrum indicate the dominant scales contributing to the variance of φ .

Throughout this paper, while visualising the contours of spectra, we have chosen to include contour levels that cover a significant amount of spectral mass, similar to the visualisation strategies employed by Lozano-Durán & Bae (2019), Deshpande, Monty & Marusic (2021) and Jiménez (2022). Changing the number of contour levels for visualisation does not alter the conclusions of the current study (see Appendix A).

The premultiplied one-dimensional energy spectra in the spanwise direction (x_3) are shown in figure 4. We also show the one-dimensional premultiplied energy spectra of streamwise velocity fluctuations of turbulent channel flow at $Re_{\tau} \approx 1000$ to understand the fundamental differences between the vertical buoyancy layers and canonical wall turbulence. The channel flow data is from Lee & Moser (2015).

In the vertical buoyancy layer, the spectral peaks occur in the outer layer at length scales of the order of the boundary layer thickness. An inner peak corresponding to nearwall (buffer layer) streaks, synonymous with canonical wall turbulence, is not observed at $x_1^+ \approx 15$ and $\lambda_{x_3}^+ \approx 100$. Qualitatively similar behaviour is observed for the constant temperature excess and heat flux thermal boundary conditions. The energy in the inner layer is mainly observed at large spanwise wavelengths, suggesting that the LSMs that are dominant in the outer layer make non-zero contributions to the TKE in the inner layer. A similar observation was also made by Maryada *et al.* (2023) while investigating the two-point correlations in wall-normal and streamwise directions.

A lack of a spectral peak corresponding to the near-wall streaks does not necessarily mean that turbulence production is absent in the inner layer at low and moderate Reynolds numbers. The shear production and buoyancy flux shown in figure 5 illustrates that turbulence is being produced in the inner layer. The shear production P_S^+ and buoyant production (buoyancy flux) P_B^+ are calculated as

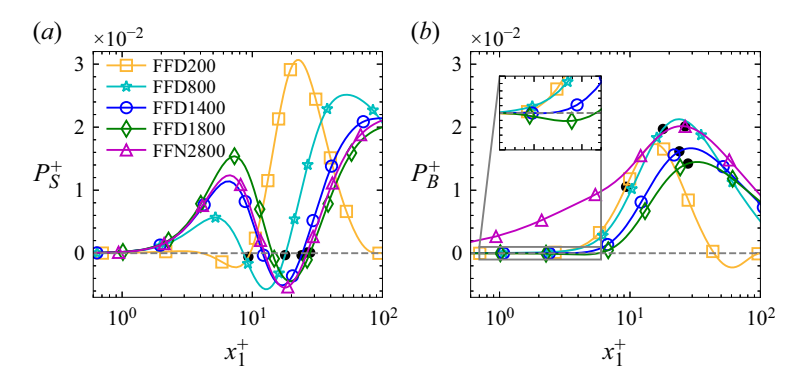


Figure 5. Profiles of (a) shear production and (b) buoyant production (buoyancy flux) at different Reynolds numbers. The location of the velocity maximum is represented using a solid black circle, demarcating the inner layer from the outer layer. Here P_S and P_B are normalised by u_τ^4/ν . Symbols and line colours are identical to figure 2.

$$P_S^+ = -\langle u_1^+ u_2^+ \rangle \frac{\partial \overline{u_2^+}}{\partial x_1^+},\tag{3.3a}$$

$$P_B^+ = g^+ \beta^+ \langle u_2^+ \vartheta^+ \rangle. \tag{3.3b}$$

Note that the streamwise turbulent heat flux and not the wall-normal turbulent heat flux features in the TKE budget equation for vertical convection (Giometto *et al.* 2017; Ke *et al.* 2023), and any subsequent references to buoyancy flux imply this quantity.

At Re = 200, the shear production is minimal and is only negative in the inner layer. At $Re \ge 800$, the shear production is positive for $x_1^+ \le 10$. Shear production is negative at the edge of the inner layer, which is related to the counter-gradient flux motions at the edge of the velocity maximum (Giometto *et al.* 2017; Maryada *et al.* 2023). Apart from an Re_{τ} dependence, there are no noticeable differences regarding shear production between the constant heat flux and the constant temperature excess boundary conditions at moderate Reynolds numbers. We emphasise that the turbulence production by shear should not be considered a signature of the ultimate regime as the inner layer is devoid of near-wall streaks (see figure 4).

Unlike shear production, the buoyancy flux strongly depends on the thermal boundary condition (figure 5b). For the constant temperature excess boundary condition, the buoyancy flux is negligible (zero or marginally negative) at $x_1^+ \lesssim 10$, while it is positive and of considerable magnitude for a constant heat flux boundary condition. At Re = 200, the buoyancy flux peak occurs beyond the maximum velocity, with minimal buoyant production in the inner layer. Negative shear production and marginal buoyancy flux at Re = 200 indicate that the near-wall turbulence is primarily due to turbulence transport from the outer layer or LSMs. At $Re \geqslant 800$, the buoyancy flux peaks approximately at maximum velocity. For the constant temperature excess boundary condition, at $800 \leqslant Re \leqslant 1400$, the buoyancy flux is positive and negligible in regions of positive shear production. At Re = 1800, the buoyancy flux is marginally negative in this region, indicating that the buoyancy flux suppresses TKE at this Reynolds number. For the FFN2800 case, the buoyancy flux is a non-zero positive value until $x_1^+ \lesssim 0.6$.

Positive shear production and buoyancy flux at $Re \ge 800$ indicate that turbulence is produced in the near-wall region even without near-wall streaks, irrespective of the thermal boundary condition.

K.R. Maryada, S.W. Armfield, M. MacDonald, P. Dhopade and S.E. Norris

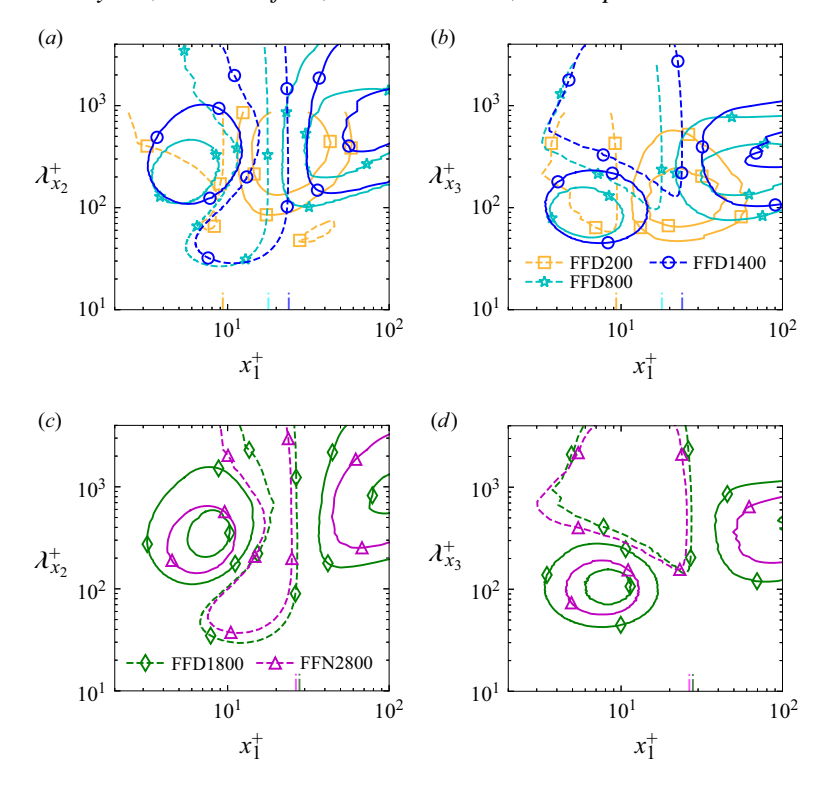


Figure 6. One-dimensional premultiplied cospectra of shear production P_S^+ in the (a,c) streamwise and (b,d) spanwise directions. Panels (a) and (b) correspond to FFD200, FFD800 and FFD1400, while panels (c) and (d) corresponds to FFD1800 and FFN2800. The contour lines are 0.15 times the minimum of FFD200 (1.1×10^{-3}) for the streamwise cospectra and -1.23×10^{-3} for spanwise cospectra), and 0.15 and 0.45 times the maximum of FFD200 (1.42×10^{-2}) for the streamwise cospectra and 2.28×10^{-2} for the spanwise cospectra). The dashed contour corresponds to the negative value, while the solid contours correspond to positive values. Vertical dash—dot lines near the abscissa indicate the edge of the inner layer. Symbols and colours are the same as figure 5.

The one-dimensional profiles in figure 5 are integral values, i.e. they represent a summation of contributions made by eddies at all possible wavelengths, providing no information on the different eddies responsible for shear and buoyant production. To better understand the different eddies that are responsible for TKE production, the premultiplied one-dimensional streamwise and spanwise cospectra of shear production and buoyant flux are shown in figures 6 and 7, respectively. The spectral formulations are

$$\widehat{P_S^+} = Re\left(-\widehat{u_1^+ u_2^+} \frac{\partial \overline{u_2}^+}{\partial x_2^+}\right),\tag{3.4a}$$

$$\widehat{P_B^+} = Re\left(g^+\beta^+ \widehat{u_2^+\vartheta^+}\right),\tag{3.4b}$$

where $u_1^+u_2^+$ and $u_2^+\vartheta^+$ represent the cross-spectrum of Reynolds shear stress and streamwise turbulent heat flux, respectively. Here, Re indicates that the real part of the cross-spectrum is considered, which gives us the cospectrum.

At Re = 200 (figures 6a and 6b), streamwise and spanwise shear production cospectra are negative in the inner layer, indicating that no wavelengths are predominantly responsible for producing TKE due to shear. For higher Reynolds numbers, regardless

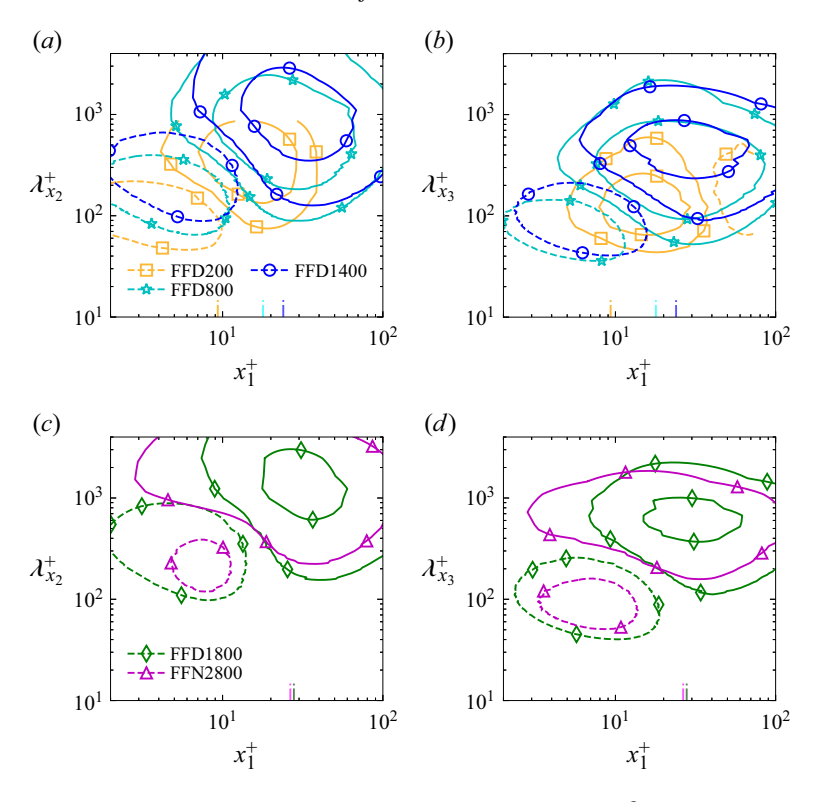


Figure 7. One-dimensional premultiplied cospectra of buoyant production $\widehat{P_B^+}$ in the (a,c) streamwise and (b,d) spanwise directions. Panels (a) and (b) correspond to FFD200, FFD800 and FFD1400, while panels (c) and (d) corresponds to FFD1800 and FFN2800. The contour lines are 0.15 times the minimum of FFD200 (1.13×10^{-3}) for the streamwise cospectra and 1.95×10^{-3} for the spanwise cospectra), and 0.15 and 0.45 times the maximum of FFD200 (8.31×10^{-3}) for the streamwise cospectra and 1.2×10^{-2} for the spanwise cospectra). The dashed contour corresponds to the negative value, while the solid contours correspond to positive values. Vertical dash–dot lines near the abscissa indicate the edge of the inner layer. Symbols and colours are the same as figure 5.

of thermal boundary conditions, streamwise and spanwise cospectra (figure 6) reveal specific wavelengths contributing to both positive and negative shear production within the inner layer. Negative shear production is associated with both short and long streamwise wavelengths, while it is only associated with long ($\lambda_{x_3}^+ \gtrsim 200$) spanwise wavelengths. Note that the magnitude of negative shear production (figure 7) is at least an order of magnitude smaller than positive shear production, and these wavelengths contribute minimally to integral negative shear production (figure 5a). The streamwise wavelength associated with positive shear production in the inner layer varies with Re_{τ} , ranging from approximately 300–450 viscous units (figures 6a and 6c). In contrast, the spanwise cospectra peak consistently at $\lambda_{x_3}^+ \approx 100$ viscous units (figures 6c and 6d) across all investigated Reynolds numbers and show little dependence on Re or the thermal boundary condition.

Interestingly, the spanwise wavelength of the most energetic contours of positive shear production is similar to canonical wall turbulence (Lee & Moser 2019). However, this constancy is not observed for the streamwise wavelength as for canonical wall turbulence, the most energetic contours of shear production are independent of Re_{τ} and are observed at $\lambda_{x_2}^+ \approx 600$ –700 (del Á lamo *et al.* 2004; Lee & Moser 2019; Jiménez 2022). This suggests that the spanwise wavelength $\lambda_{x_3}^+ \approx 100$ for the near-wall shear production spectral peak

is not limited to canonical wall turbulence. Its signatures are evident in turbulent vertical natural convection at moderate Re_{τ} , which has been hitherto undetected (discussed further in § 3.5).

In figure 7, for all cases, certain streamwise wavelengths exhibit positive buoyancy flux while others exhibit negative buoyancy flux in the inner layer. Positive buoyancy flux contributes to TKE production, while negative buoyancy flux contributes to its suppression.

At Re = 200, in terms of spanwise cospectra, the buoyancy flux is negligible. For Re > 200, the dominant streamwise and spanwise wavelengths of negative buoyancy flux are similar. The wavelengths of most energetic contours that contribute negatively to the buoyancy flux are $\lambda_{x2}^+ \approx 250$ –450 and $\lambda_{x3}^+ \approx 100$, which are similar to the energetic contours of positive shear production in the inner layer. A similar comparison cannot be made at Re = 200 as positive shear production is not dominant in the inner layer.

The buoyancy flux is linearly proportional to the streamwise turbulent heat flux; therefore, the one-dimensional cospectra in figure 7 also provide information on the correlation between streamwise velocity and temperature fluctuations at different wavelengths. The positive values in figure 7 imply that the streamwise velocity and temperature fluctuations are positively correlated, while a negative value implies that these are negatively correlated.

The positive correlation between the streamwise velocity and temperature fluctuations suggests that high-speed eddies are generally composed of higher temperatures, while low-speed eddies are generally of lower temperatures. A positive correlation is observed at large streamwise and spanwise scales in the inner layer, suggesting that these are synonymous with the LSMs observed in the outer layer (Maryada *et al.* 2023). At these wavelengths, eddies with higher temperatures experience greater buoyancy and travel faster than those with lower temperatures.

The negative correlation in the inner layer suggests that slow-moving eddies are generally composed of high temperatures, while fast-moving eddies have low temperatures. At first glance, this seems counterintuitive as it suggests buoyancy is actively suppressing turbulence at these scales, particularly since the current flow is solely driven by buoyancy. At these wavelengths, at Re > 200, the magnitude of shear production is at least an order of magnitude greater than the buoyancy flux (see figures 4 and 7), implying that these wavelengths are mostly controlled by shear. As the shear production is positive, the Reynolds shear stress is mainly composed of Q2 $(u_1 > 0, u_2 < 0, as$ we define x_1 as wall-normal and x_2 as streamwise/vertical directions) and Q4 ($u_1 < 0, u_2 > 0$) events (Wallace 2016). These events mix the low-speed fluid next to the wall and the high-speed fluid slightly away from it. Due to a heated wall, the fluid next to it is at a higher temperature than the fluid farther away. Hence, the low-speed fluid is associated with higher temperatures, and the high-speed fluid is associated with lower temperatures, mirroring forced convection heat transfer. This indicates that at small wavelengths, the u_2 eddies in vertical natural convection boundary layers transport heat in the same fashion as forced convection. We call this induced heat flux.

For a constant temperature excess boundary condition, at Re = 200, shear production is not dominant in the inner layer, resulting in negligible induced heat flux. However, as Re increases beyond 200, a substantial positive shear production emerges, resulting in an appreciable induced heat flux (as illustrated in figures 6 and 7). The one-dimensional profile in figure 5 represents the integral of shear production and buoyancy flux across all wavelengths. In the range of $800 \le Re \le 1400$, this integral is positive or approximately zero within the inner layer, indicating that the magnitude of the positive streamwise turbulent heat flux is either larger than or comparable to the magnitude of the induced heat

Case	Domain size $(x_1^+ \times x_2^+ \times x_3^+)$	$N_{x_1} \times N_{x_2} \times N_{x_3}$	Δx_{1w}^+	$\Delta x_{1\delta_{bl}}^+$	Δx_2^+	Δx_3^+
FSD1400	$3235 \times 986 \times 493$	$355 \times 200 \times 100$	0.43	5.99	4.93	4.93
RSD1400	$166 \times 1060 \times 530$	$100 \times 200 \times 100$	0.46	2.02	5.30	5.30
R ₂ SD1400	$337 \times 982 \times 491$	$200 \times 200 \times 100$	0.43	2.16	4.91	4.91
RLD1400	$166 \times 3172 \times 529$	$120 \times 600 \times 100$	0.46	1.53	5.29	5.29

Table 2. Simulation settings for DNS of the minimal domain at Re = 1400. Here, the domain and grid sizes are normalised using the viscous length scale. For RSD1400 and R₂SD1400, $\Delta x_{1\delta_{bl}}^+$ corresponds to the cell size at the edge of the domain; for FSD1400, $\Delta x_{1\delta_{bl}}^+$ corresponds to the cell size at the edge of the boundary layer. See the text for the notation used for case names.

flux. The magnitude of the induced heat flux in the inner layer grows relative to the positive buoyancy flux with increasing Re. This dominance of the negative buoyancy flux causes the integral (the one-dimensional profile) to become negative at Re = 1800. Consequently, depending on the Reynolds number, the mean streamwise turbulent heat flux can exhibit negative, near-zero or positive values, with its sign determined by the prevailing turbulent processes.

These findings clarify the longstanding questions regarding the *Re*-dependence and the underlying physical mechanisms responsible for negative streamwise turbulent heat flux and Reynolds shear stress in the inner layer of vertical natural convection boundary layers (To & Humphrey 1986; Abedin *et al.* 2009; Nakao, Hattori & Suto 2017).

Despite the buoyancy flux being positive for FFN2800, in figure 7, we see that the buoyant production at $\lambda_{x_3}^+ \lesssim 300$ is similar for the constant heat flux and constant temperature excess boundary conditions (dominated by negative values). This, combined with similarity in shear production, indicates a universal turbulence production mechanism in the near-wall region of buoyancy layers, which is examined in the following sections.

3.3. Self-sustaining nature of inner-layer turbulence at moderate Reynolds numbers

As evident from § 3.1, at low and moderate *Re*, turbulence is mainly observed in the outer layer of vertical buoyancy layers. We know that the outer layer is composed of streamwise-elongated LSMs, which carry a significant portion of the TKE and Reynolds shear stress. Significant wall-normal coherence is also present, with the LSMs being strongly correlated between the inner and the outer layers (Maryada *et al.* 2023). There is an appreciable nonlinear wall-normal transport of turbulence from the outer to the inner layer in a vertical natural convection boundary layer flow (Giometto *et al.* 2017; Ke *et al.* 2023). Moreover, it is often argued that this wall-normal transport of turbulence is the predominant way in which turbulence is maintained in the inner layer at moderate Reynolds numbers.

In spite of all these observations, in this section, based on the fact that turbulence is produced locally in the near-wall region at moderate Reynolds numbers (see § 3.2), it is investigated whether the inner-layer turbulence is autonomous and self-sustaining, i.e. whether it can sustain even if the LSMs and outer-layer flow are disturbed heavily. To this end, motivated by the studies of Jiménez & Moin (1991), Jiménez & Pinelli (1999), Hwang (2013) and Jiménez (2022), four different numerical simulations using minimal domains were performed at Re = 1400, which is sufficient to observe the adequate turbulence production in the inner layer (see figures 5, 6 and 7). The relative sizes of the minimal (truncated) domains to FFD1400 are shown in figure 8, and the corresponding details are given in table 2.

The four numerical simulations feature domains smaller than FFD1400 in the streamwise and spanwise directions (figure 8). Decreasing the streamwise and spanwise

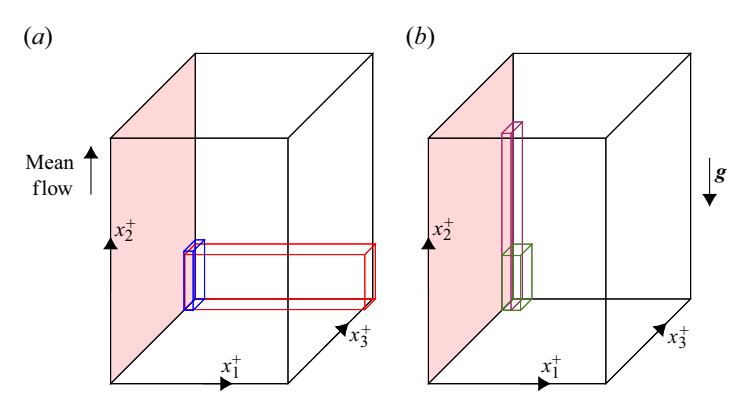


Figure 8. The relative sizes of the minimal domains to the FFD1400 domain (large black box), which are shown to scale. In panel (a), the red box represents FSD1400, and the blue box represents RSD1400. The magenta and green boxes in panel (b) represent RLD1400 and R₂SD1400, respectively.

lengths restricts the largest streamwise and spanwise wavenumbers that can be captured in the domain. The wall-normal domain size for FSD1400 is comparable to FFD1400 (figure 8a). Similar to FFD1400, an open-type boundary condition is used at the wall-normal far-field boundary for the FSD1400 simulation. With this DNS dataset, we are interested in investigating whether the LSMs need to be adequately resolved to replicate the second-order statistics of motions smaller than LSMs.

To drastically modify the outer layer turbulence and bulk flow, in RSD1400, R₂SD1400 and RLD1400, the wall-normal domain is truncated to severely inhibit the outer flow (figure 8). In RSD1400 and RLD1400, the wall-normal domain is restricted to $x_1^+ \approx 170$, while in R₂SD1400, it is restricted to $x_1^+ \approx 340$, which are smaller than the boundary layer thickness at Re = 1400 (boundary layer thickness as observed in the FFD1400 simulation). In these minimal domains, at the wall-normal boundary (far-field boundary condition), a free-slip wall ($\tilde{u}_1 = \partial \tilde{u}_2/\partial x_1 = \partial \tilde{u}_3/\partial x_1 = 0$) with a constant temperature $\tilde{\vartheta} = 0$ boundary condition is applied, replacing the opening boundary condition used for FFD1400 and FSD1400. This boundary condition was specifically chosen as it inhibits the wall-normal motions (u_1 fluctuations), thereby directly affecting $\langle u_2 u_2 \rangle$, as $\langle u_1 u_2 \rangle$ and $\langle u_2 u_2 u_1 \rangle$ feature in turbulent production and transport. A free-slip wall affects turbulence differently than a standard no-slip wall, as it enforces $\tilde{u}_1 = \partial \tilde{u}_2/\partial x_1 = \partial \tilde{u}_3/\partial x_1 = 0$, compared with a no-slip wall where $\tilde{u}_i = 0$. Consequently, these minimal domains cannot be directly related to internal natural convection or natural convection in enclosures.

Note that RSD1400 and RLD1400 are similar in the wall-normal and spanwise directions but only differ in the streamwise direction, with RLD1400 being almost three times bigger than RSD1400. We use this simulation to understand the statistics of large scales in the inner layer.

The outer-layer turbulence/bulk flow can be suppressed or modified using several methods that are different from the one employed in the current study (e.g. the spectral filtering approaches of Jiménez & Pinelli (1999), Hwang (2013) and Jiménez (2022) or the damping approach of MacDonald *et al.* (2017) for turbulent channels). Here, we are not interested in understanding how different methods suppress or modify the bulk flow. We also emphasise that the aim of these numerical experiments is not to reproduce the one-point statistics in minimal domains accurately, as is usually done in turbulent channels (e.g. MacDonald *et al.* 2017; Yin, Huang & Xu 2018). Instead, we are only interested in understanding how a modified bulk affects turbulence in the inner layer. If the spectral

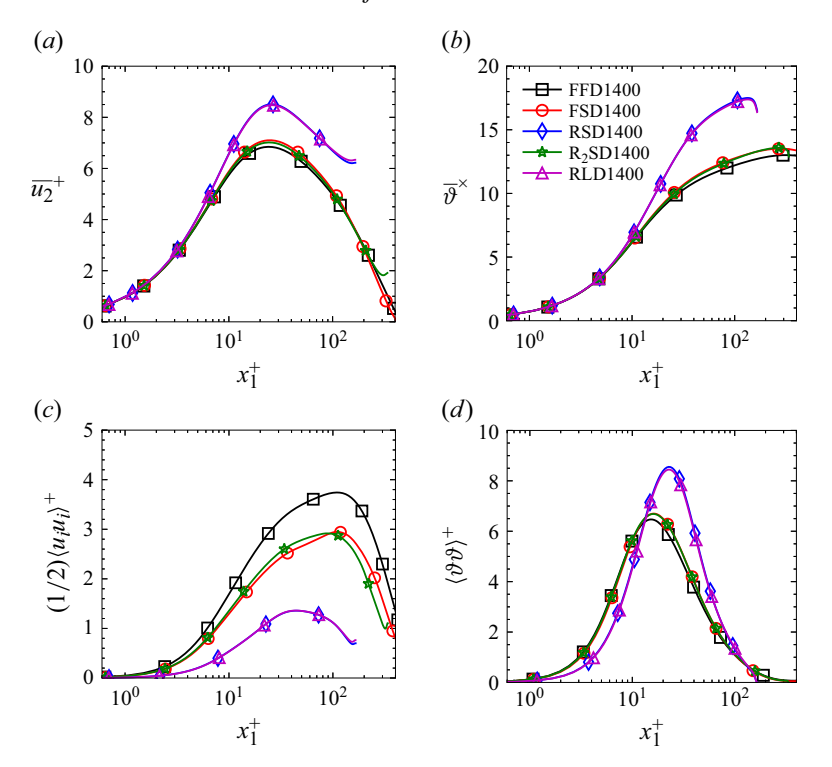


Figure 9. Mean flow and one-point statistics of the minimal and full domains at Re = 1400. Panel (a) corresponds to mean streamwise velocity $\overline{u_2}^+$, panel (b) corresponds to mean temperature field ϑ^\times , panel (c) corresponds to TKE and panel (d) corresponds to buoyancy variance $\langle \vartheta \vartheta \rangle^+$.

energy signature of the resolved turbulence in the minimal domains is similar to that of FFD1400, then we can infer that the LSMs and outer flow only play a marginal role in the near-wall turbulence dynamics. If it is the contrary, we can deduce that the inner-layer turbulence significantly depends on the bulk flow.

For all the minimal domains, the simulations were initialised using the turbulent flow field of the FFD1400 simulation. The FSD1400 and RLD1400 were run for over 7.5×10^4 viscous time units before averaging, while the RSD1400 and R₂SD1400 were run for over 10×10^4 viscous time units before averaging to ensure that turbulence did not decay for large simulation times. The statistics reported are averaged over five buoyancy time periods in all cases. The rest of this section is dedicated to examining the one-point and spectral statistics.

The mean streamwise velocity fields of the minimal domains and FFD1400 are shown in figure 9(a). The mean streamwise velocity fields of FSD1400 and R₂SD1400 are very similar to those of FFD1400 for most of the boundary layer. On the other hand, the mean streamwise velocity fields of RSD1400 and RLD1400 with very minimal wall-normal domain extents are different from FFD1400 but are identical to each other. The mean temperature field is shown in figure 9(b), and no noticeable differences until $x_1^+ \lesssim 10$ for all cases. This is expected as diffusion primarily governs the mean temperature field in the near-wall region. At $x_1^+ > 10$, FSD1400 and R₂SD1400 deviate marginally from FFD1400 while RSD1400 and RLD1400 deviate significantly. Like the mean streamwise velocity field, the mean temperature fields of RSD1400 and RLD1400 are identical to each other.

The TKE profiles are shown in figure 9(c). The TKE magnitude is lower in minimal domains than in the full domain, implying that the LSMs make a non-negligible contribution to velocity variances across almost the entire thickness of the boundary layer. Regarding buoyancy variance (figure 9d), FSD1400 and R₂SD1400 are in excellent agreement with FFD1400 until $x_1^+ \lesssim 10$; however, a mild deviation is seen at larger wall-normal distances. Cases RSD1400 and R₂SD1400 are significantly different from the reference case of FFD1400, exhibiting an increased magnitude of thermal fluctuations. Like the mean flow, the TKE and buoyancy variances of RSD1400 and RLD1400 are identical, indicating that the streamwise length of the domain does not influence these statistics. Instead, it is the truncated wall-normal domain that affects it.

As the velocity and buoyancy variances represent the integral of different eddies at all wavelengths, investigating the spectral properties would provide a better metric to quantify the independence of inner-layer turbulence. To this end, we investigate the premultiplied two-dimensional spectra of velocity fluctuations to investigate how the minimal domains affect the different eddies (different Fourier components). Using two-dimensional spectra mitigates the issue of aliasing in the homogeneous directions (Tennekes & Lumley 1972), and following Jiménez *et al.* (2004), Chandran *et al.* (2017) and Hwang *et al.* (2020), we plot the two-dimensional spectra in the logarithmic Cartesian space. It is shown in figure 10, where the spectra are averaged across the entire thickness of the inner layer.

Figure 10 shows the premultiplied two-dimensional spectra of velocity and buoyancy fluctuations. Although the FSD1400 case is too small to fully resolve LSMs in both streamwise and spanwise directions, the resolved portion of its spectra in the minimal domain closely matches the full domain's spectra. This indicates that the minimal domain can accurately capture the wavelengths of the resolved turbulent fluctuations, even if LSMs are not properly resolved. Consequently, the discrepancy in velocity and buoyancy variances between FSD1400 and FFD1400 (figure 9) primarily stems from FSD1400 lacking energy from unresolved LSMs, rather than a fundamental alteration of small-wavelength structures in the near-wall region between the two domains.

Now consider RLD1400, RSD1400 and R₂SD1400 where a limited wall-normal extent and a free-slip boundary alter outer-layer turbulence. The energetic contours of R₂SD1400 are in good agreement with those of FSD1400 (domain only truncated in the streamwise and spanwise directions) and FFD1400 (the full domain, i.e. no truncation in any direction), suggesting that beyond a specific wall-normal location, the bulk flow only marginally affects the small scales in the inner layer. However, the same cannot be said for RLD1400 and RSD1400, which have an even more limited wall-normal domain extent. The effect of the free-slip boundary condition in the outer layer is felt deep into the inner layer. Substantial differences are observed in buoyancy and all three velocity components compared with FFD1400. In spite of this, similar to the one-point statistics shown in figure 9, the spectra of RLD1400 and RSD1400 are in excellent agreement with each other, reaffirming that the wall-normal domain size has a more significant impact on turbulence than streamwise domain truncation.

Despite all the differences in spectra, the long and narrow streamwise velocity modes of RLD1400 and RSD1400 ($\lambda_{x_2}^+ \gg \lambda_{x_3}^+$ and $\lambda_{x_3}^+ \lesssim 200$) are in very good agreement with FFD1400, suggesting that these scales survive even if the outer layer is drastically different. This is only observed for streamwise velocity fluctuations, not other velocity and buoyancy fluctuations. Therefore, the long and narrow structures of streamwise velocity fluctuations in the inner layer must be primarily due to local flow processes and not solely due to LSMs.

Figure 11 shows the premultiplied two-dimensional cospectra of shear production and buoyancy flux of the minimal domains and FFD1400. The spectral signature of shear production and buoyancy flux of FSD1400 and $R_2SD1400$ is similar to FFD1400, which

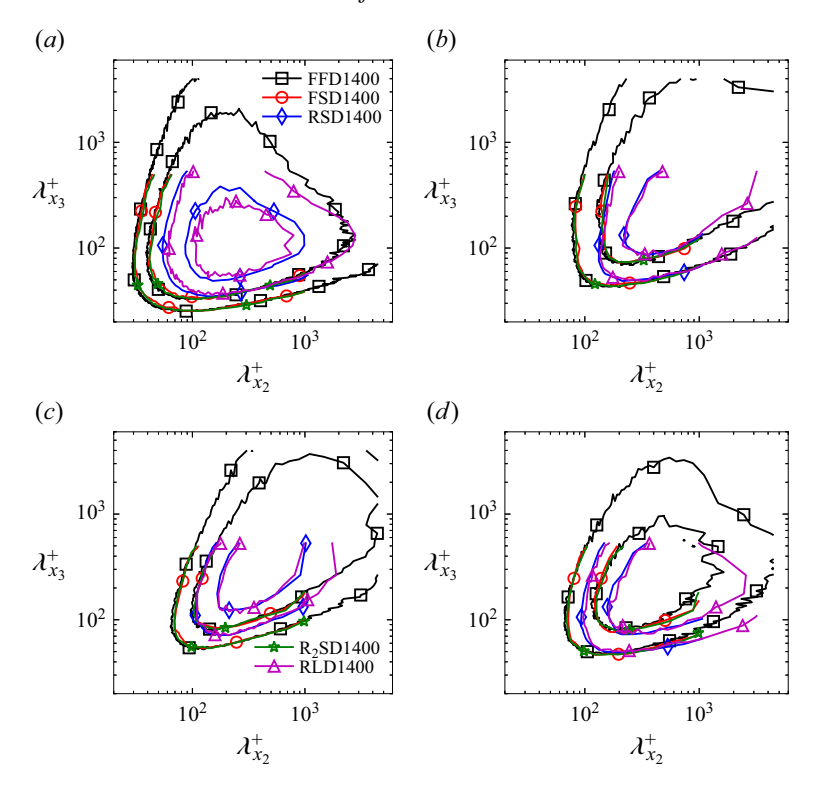


Figure 10. Premultiplied two-dimensional energy spectra of velocity fluctuations averaged across the inner layer. The panels correspond to fluctuations of (a) wall-normal velocity, (b) streamwise velocity, (c) spanwise velocity and (d) temperature. The contour lines are 0.15 and 0.45 times the maximum value of RSD1400 (6.8 \times 10⁻³, 1.11 \times 10⁻¹, 9.01 \times 10⁻² and 7.36 \times 10⁻¹ for wall-normal velocity, streamwise velocity, spanwise velocity and temperature energy spectra, respectively). Symbols and colours are the same as figure 9. The energy is normalised using viscous units.

is our largest domain at Re = 1400, indicating that the shear production and buoyancy flux (both positive and negative) at these scales in the inner layer do not depend on whether the LSMs and the outer bulk flow are resolved correctly. Interestingly, even in RLD1400 and RSD1400, the contours of positive shear production and negative buoyancy flux are in fair agreement with FFD1400 except at small streamwise and spanwise wavelengths, despite the energy spectra of streamwise, wall-normal and buoyancy fluctuations exhibiting significant differences in figure 10. This strongly suggests that the turbulence production in the inner layer is autonomous and depends only marginally on outer-layer dynamics.

The effect of domain size on the Nusselt number is discussed in Appendix B. However, this is not examined in greater detail as the primary aim of the current study is to understand the near-wall fluctuations and not the behaviour of mean wall quantities.

Moreover, for all cases, the turbulence does not decay even after long integration times, indicating that the turbulence in the inner layer is self-sustaining and autonomous, at least on a fundamental level. Such self-sustaining behaviour of near-wall and outer-layer motions was previously observed in the buffer layer, logarithmic and the core region of turbulent channels (Jiménez & Moin 1991; Jiménez & Pinelli 1999; Jiménez *et al.* 2004; Flores & Jiménez 2010; Cossu & Hwang 2017). These observations indicate that the structural elements of canonical wall turbulence are present in vertical buoyancy-driven boundary layers at moderate *Re.* However, their presence is not apparent in

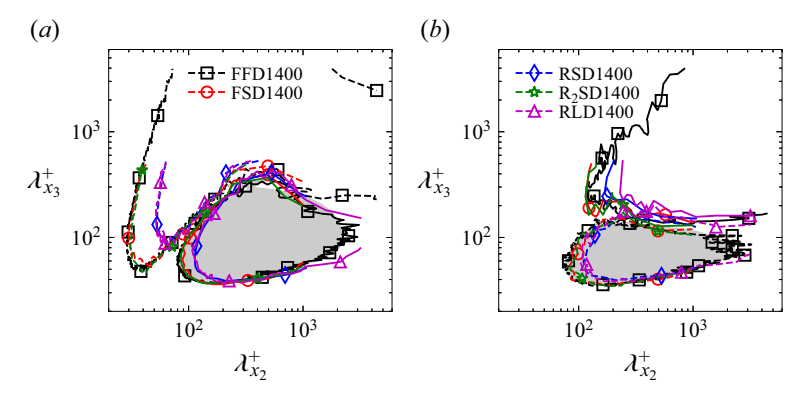


Figure 11. Two-dimensional premultiplied cospectra of (a) shear production $\widehat{P_S^+}$ and (b) buoyant production $\widehat{P_B^+}$ of full and minimal domains averaged in the inner layer. The contour lines are 0.15 times the minimum $(-1.42 \times 10^{-4} \text{ for shear production and } -2.1 \times 10^{-4} \text{ for buoyancy flux})$ and maximum $(-1.56 \times 10^{-3} \text{ for shear production and } 5.7 \times 10^{-4} \text{ for the buoyancy flux})$ values of RSD1400. Solid contours represent a positive value, while the dashed contour corresponds to a negative value. The grey-shaded region represents positive shear production and negative buoyancy flux (induced heat flux) of FFD1400. Symbols and colours are the same as figure 9.

the premultiplied one-dimensional energy spectra of streamwise fluctuations (figure 4). Instead, spectral signatures consistent with canonical wall turbulence are evident in shear production. Therefore, the inner-layer turbulence of vertical convection in the classical regime, so long as turbulence is produced locally, can be thought of as having a combination of turbulence structures representative of canonical wall turbulence and other motions specific to vertical convection. This similarity between the current flow configuration and canonical wall turbulence is further discussed in §§ 3.4 and 3.5.

It should be noted that the present similarity is observed without the distance-from-the-wall-scaled eddies (the spectra of u_2 in figure 4 does not scale linearly with respect to wall-normal distance as in canonical wall turbulence (Hwang 2015; Lee & Moser 2019)), implying that the scale-based self-sustaining process observed here is not merely a consequence of attached eddies.

This section has shown that small scales in the near-wall region are self-sustaining and autonomous. Consequently, very large computational domains are not required for numerical simulations; minimal domains can be effectively used to investigate the low-order statistics of small-scale motions in the near-wall region of turbulent vertical buoyancy layers (also see Appendix B regarding Nusselt number).

3.4. Near-wall turbulence in the ultimate regime

Based on the above observations regarding the autonomous nature of turbulence in the inner layer (§ 3.3), we use minimal domains to investigate the vertical buoyancy layer at a significantly higher Re to understand the inner layer turbulence in the ultimate regime. The ultimate regime corresponds to Reynolds numbers where a well-developed peak is observed at $x_1^+ \approx 15$ and $\lambda_{x_3}^+ \approx 100$ in the one-dimensional spanwise spectra of streamwise velocity fluctuations (Ng *et al.* 2017; Ke *et al.* 2023). We report results at Re = 3500 as it was found to be sufficiently high to observe a well-developed inner peak in the one-dimensional spanwise spectra of streamwise velocity fluctuations.

We have performed five numerical simulations with different boundary conditions and domain sizes, whose details are summarised in table 3. Like the classical regime (table 1),

Case	Domain size $(x_1^+ \times x_2^+ \times x_3^+)$	$N_{x_1} \times N_{x_2} \times N_{x_3}$	Δx_{1w}^+	$\Delta x_{1\delta_{bl}}^+$	Δx_2^+	Δx_3^+
FLD3500	$4694 \times 2380 \times 873$	$360 \times 500 \times 184$	0.33	14.08	4.76	4.76
FSD3500	$5079 \times 1226 \times 450$	$350 \times 250 \times 92$	0.34	11.48	4.89	4.89
FSN3500	$5137 \times 1240 \times 455$	$350 \times 250 \times 92$	0.34	10.90	4.94	4.94
RSD3500	$308 \times 1302 \times 478$	$100 \times 250 \times 92$	0.36	5.37	5.19	5.19
RSN3500	$308 \times 1300 \times 477$	$100 \times 250 \times 92$	0.36	5.36	5.18	5.18

Table 3. Simulation settings for DNS of the minimal domain at Re = 3500. Here, the domain and grid sizes are normalised using the viscous length scale. For RSD3500 and RSN3500, $\Delta x_{1\delta_{bl}}^+$ corresponds to the cell size at the edge of the domain; for FLD3500, FSD3500 and FSN3500, it corresponds to the cell size at the edge of the boundary layer. See the text for the notation used for case names.

both constant temperature excess and constant heat flux boundary conditions were investigated to understand the effect of thermal boundary conditions. Following Moin & Kim (1982), the two-point correlations of the velocity fluctuations were computed in the streamwise and spanwise directions for all cases, and it was found that the streamwise and spanwise lengths of all the domains were not sufficiently long to resolve the largest scales of turbulence accurately. However, from § 3.3, we know that the scales smaller than the largest scales of motion do not significantly depend on the latter. Therefore, based on these observations, one can use minimal domains to understand small scales in the near-wall region.

At the heated wall, a constant temperature excess boundary condition ($\tilde{\vartheta}=1$) was used for FLD3500, FSD3500 and RSD3500, while a constant heat flux boundary condition was used for FSN3500 and RSN3500. However, unlike FFN2800, the non-dimensional temperature gradient imposed at the heated wall was not unity but was equal to the mean temperature gradient observed in FSD3500. Using the mean temperature gradient of a constant temperature excess boundary condition ensures that Re_{τ} is comparable for both thermal boundary conditions. This was done to isolate the effect of the thermal boundary condition.

The wall-normal domain is sufficiently large in FLD3500, FSD3500 and FSN3500 to avoid any influence of the far-field boundary condition. In these simulations, an open-type boundary condition was used at the wall-normal far-field boundary. In RSD3500 and RSN3500, the domain is restricted to only six units (units defined using the current non-dimensionalisation described in § 2, which is ≈ 300 viscous units) in the wall-normal direction. Similar to RSD1400 and RLD1400 outlined in § 3.3, for RSD3500 and RSN3500, the opening boundary condition was replaced with a free-slip wall ($\tilde{u}_1 = \partial \tilde{u}_2/\partial x_1 = \partial \tilde{u}_3/\partial x_1 = 0$) having a non-dimensional temperature $\tilde{\vartheta} = 0$. This wall-normal domain size cannot accurately capture the boundary layer flow and would severely inhibit the outer layer turbulence, allowing us to discern the autonomous nature of the inner layer turbulence.

Similar to what is observed at Re = 1400, the mean flow and one-point statistics differ across different domain sizes, shown in Appendix C. The statistical properties of the eddies are of interest and, hence, are the subject of focus in this section.

In figure 12, we plot the one-dimensional energy spectra of streamwise velocity fluctuations in the spanwise direction to determine whether the buoyancy layer has transitioned into the ultimate regime. Note that the inner layer is deemed to be turbulent in the sense of Prandtl and von Kármán if this spectrum exhibits a peak at $x_1^+ \approx 15$ and $\lambda_{x_3}^+ \approx 100$ (Ke *et al.* 2023). Usually, the transition from the classical to the ultimate regime in vertical convection is defined using the mean Nusselt number, with the classical and

K.R. Maryada, S.W. Armfield, M. MacDonald, P. Dhopade and S.E. Norris

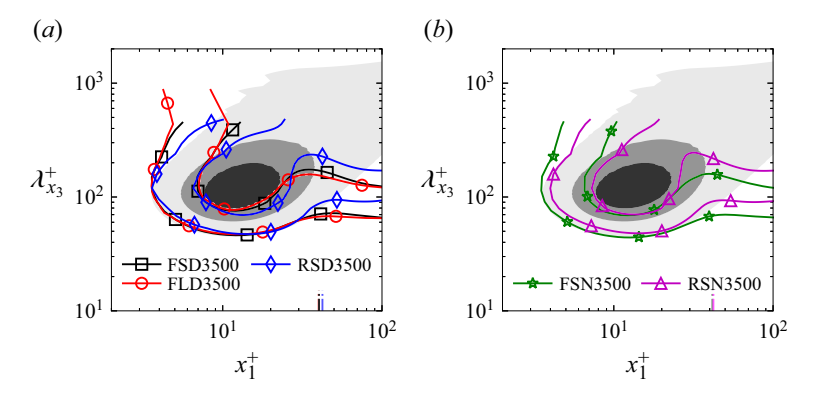


Figure 12. One-dimensional premultiplied energy spectra of streamwise velocity fluctuations in the spanwise direction at Re = 3500. Panel (a) shows FSD3500 (black squares), FLD3500 (red circles) and RSD3500 (blue diamonds), while panel (b) shows FSN3500 (green stars) and RSN3500 (magenta triangles). Vertical dash-dot lines near the abscissa indicate the edge of the inner layer. Also shown in panels (a) and (b) is that of a turbulent channel flow at $Re_{\tau} \approx 1000$ (LM1000), which is from Lee & Moser (2015). The contour lines are 0.15 and 0.45 times the maximum value of RSD3500 (0.76). Similar to figure 4, the shaded contours correspond to 1, 2, 3 and 4 (light to dark) for LM1000. The energy is normalised using viscous units.

ultimate regimes exhibiting different power-law scalings (Wells & Worster 2008; Ng et al. 2015, 2017). However, it is clear from Appendix B that at constant Re, the domain size affects the Nusselt number. Therefore, using a mean quantity such as the Nusselt number would not accurately demarcate the transition from the classical to the ultimate regime, especially when using minimal domains. Moreover, it is well known that the change in the power-law scaling of the Nusselt number is gradual. Despite this, the formation of the near-wall peak in the one-dimensional energy spectra of streamwise velocity fluctuations is much more consistent (Ke et al. 2023). Hence, we rely on the near-wall peak to distinguish the classical and ultimate regimes.

The differences between figures 12 and 4 are immediately evident. Unlike what is observed at $200 \le Re \le 2800$, irrespective of the thermal boundary condition, a well-developed spectral peak is observed at $\lambda_{x_3}^+ \approx 100$ and $x_1^+ \approx 15$ at Re = 3500. The wall-normal location and the spanwise wavelength of the spectral peak are similar to the inner site of canonical wall turbulence, which corresponds to the near-wall streaks (Kline *et al.* 1967; Hutchins & Marusic 2007; Lee & Moser 2015; Hwang *et al.* 2020). Therefore, at Re = 3500, the inner layer is turbulent in the sense of Prandtl and von Kármán (Ng *et al.* 2017; Ke *et al.* 2023). The magnitude of the vertical buoyancy layer contours and channel flow shown in figure 12 are not expected to match as both flows are driven differently (Ke *et al.* 2023). However, the similarity in the shape of the contours indicates a direct correspondence in terms of the spanwise wavelength, with the energy only being offset by some amount, which is likely a function of Re.

Figure 13 shows the snapshots of streamwise velocity fluctuations at $x_1^+ \approx 15$ for cases FFD1400 and FLD3500, which can be related to the spectra shown in figures 4 and 12. The streamwise velocity fluctuations have a relatively 'coarse' structure in figure 13(a), corresponding to FFD1400. A streamwise-elongated streaky structure of positive and negative streamwise velocity fluctuations is absent. However, for FLD3500 (figure 13b), the streamwise velocity fluctuations exhibit a 'finer' structure than that of FFD1400, with the positive and negative streamwise velocity fluctuations now being organised into an alternating streak-like pattern. The spanwise wavelength of these streaky structures is approximately 100 viscous units, corresponding to the spectral peak in figure 12. The

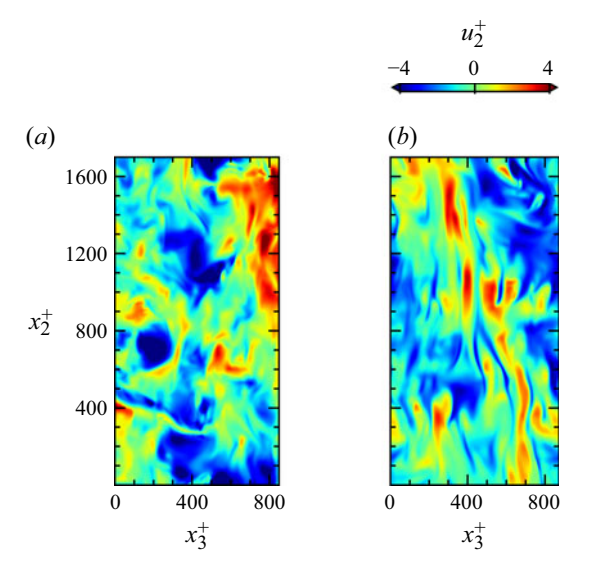


Figure 13. The streamwise–spanwise plane at $x_1^+ \approx 15$, showing the contours of fluctuating streamwise velocity at different Reynolds numbers. Panel (a) shows FFD1400 (Re = 1400, classical regime) while panel (b) shows FLD3500 (Re = 3500, ultimate regime). Only a portion of the FFD1400 and FLD3500 domains is shown.

change in the structure of the streamwise velocity fluctuations with increasing *Re* was also observed in unstratified turbulent vertical natural convection boundary layers (Ng *et al.* 2017; Ke *et al.* 2023).

In shear-driven turbulence (e.g. canonical wall turbulence or homogeneous shear turbulence), a streaky structure of streamwise velocity fluctuations emerges primarily due to the high shear rates (Lee, Kim & Moin 1990). The emergence of such a streaky structure in the present case indicates that an increase in the Reynolds number increases the shear rate in the inner layer, irrespective of the domain size and thermal boundary condition. The increase in the shear rate can either be due to local processes or due to the driving force of the bulk flow.

The spectral similarity across the different domain sizes in figure 12 indicates LSMs need not be fully resolved for accurate second-order statistics for small-scale motions in the inner layer. Near-wall streaks are present regardless of the thermal boundary condition (comparing FSD3500 and FSN3500) and even when the outer flow is severely modified (comparing RSD3500, FSD3500 and FLD3500, as well as RSN3500 and FSN3500). The turbulence is self-sustaining at these spanwise wavelengths, and the LSMs are not fundamental features of turbulence in the inner layer of vertical convection. This strongly suggests that local processes are sufficient to generate high shear rates and that the bulk flow need not drive the flow for the inner layer to become turbulent.

The results presented so far in this section and § 3.3 demonstrate that the scale-based self-sustaining turbulence is not limited to canonical wall turbulence but is also present in buoyancy-driven flows such as the vertical buoyancy layer, which has not been reported until now.

The two-dimensional premultiplied energy spectra of velocity and buoyancy fluctuations are shown in figure 14. Like figure 10, the energy spectra are averaged across the inner layer. The energetic contours of FSD3500 and FSN3500, as well as RSD3500 and RSN3500, are similar, suggesting that the thermal boundary does not significantly

K.R. Maryada, S.W. Armfield, M. MacDonald, P. Dhopade and S.E. Norris

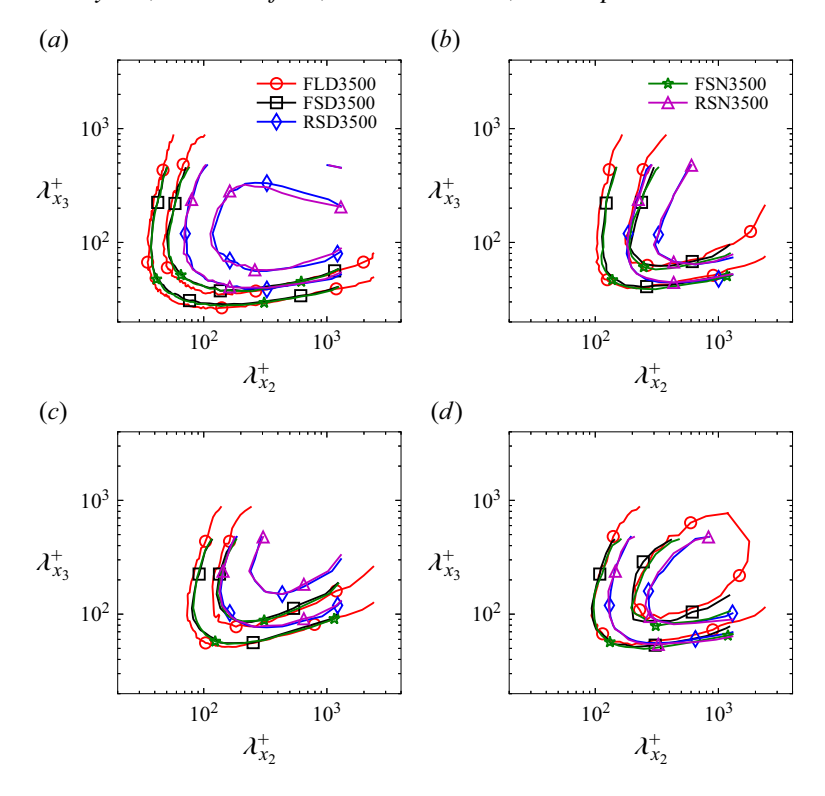


Figure 14. Premultiplied two-dimensional spectra of velocity and buoyancy fluctuations averaged across the inner layer at Re = 3500. Here, panels correspond to fluctuations of (a) wall-normal velocity, (b) streamwise velocity, (c) spanwise velocity and (d) buoyancy. The contour lines are 0.15 and 0.45 times the maximum value of RSD3500 (7.38 × 10^{-3} , 1.29×10^{-1} , 6.44×10^{-2} and 1.08 for wall-normal velocity, streamwise velocity, spanwise velocity and temperature energy spectra, respectively). Symbols and colours are the same as figure 12. The energy is normalised using viscous units.

influence the statistical eddy behaviour so long as the wall heat flux is comparable. The resolved scales in FSD3500 are in excellent agreement with FLD3500 (FSD3500 and FLD3500 have identical boundary conditions except that FLD3500 is twice as long and twice as wide as FSD3500), indicating that the small scales do not strongly depend on large scales.

For RSD3500 and RSN3500, the premultiplied two-dimensional spectra of wall-normal and spanwise velocity fluctuations and buoyancy fluctuations deviate from FSD3500, FLD3500 and FSN3500 at all the streamwise and spanwise wavelengths (figures 14a, 14c and 14d). However, the premultiplied two-dimensional spectrum of streamwise velocity fluctuations of RSD3500 and RSN3500 exhibit similarities with FSD3500, FLD3500 and FSN3500 at $\lambda_{x_2}^+ \lesssim 100$ and $\lambda_{x_2}^+ \gg \lambda_{x_3}^+$ (figure 14b), suggesting that long and narrow streamwise velocity eddies are autonomous to the inner layer, similar to what is observed at Re = 1400 (figure 10). Note that $\lambda_{x_2}^+ \approx 1000$ and $\lambda_{x_3}^+ \approx 100$ correspond to streamwise and spanwise wavelengths of the near-wall streaks (hence, the similarity observed in figure 12).

The premultiplied one-dimensional shear production cospectra are shown in figure 15. In the inner-layer, the positive shear production peaks at $\lambda_{x_2}^+ \approx 600\text{-}700$ and $\lambda_{x_3}^+ \approx 100$. These wavelengths correspond to Q2 and Q4 events of Reynolds shear stress. The spanwise cospectral peak is observed at $\lambda_{x_3}^+ \approx 100$, which is the same as what is observed at $800 \leqslant Re \leqslant 2800$ (figure 6). The constancy of the spanwise wavelength at $800 \leqslant Re \leqslant 3500$

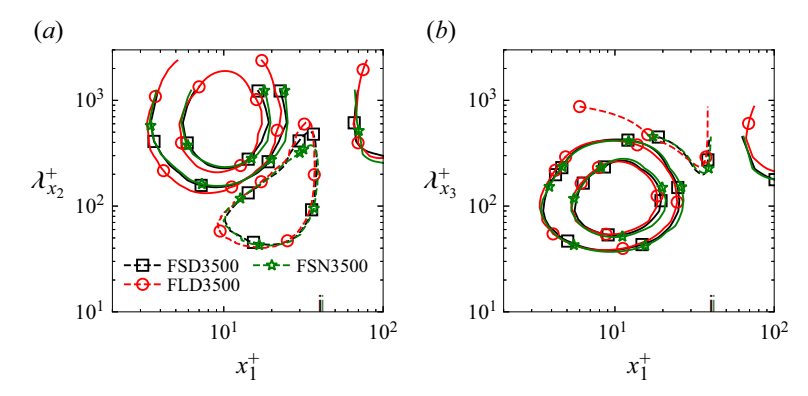


Figure 15. One-dimensional premultiplied cospectra of shear production P_S^+ in the streamwise (a) and spanwise (b) directions at Re = 3500. The contour lines are 0.15 times the minimum of FSD3500 (1.27 × 10⁻³) and 0.15 and 0.45 times the maximum of FSD3500 (2.13 × 10⁻²). The dashed contour corresponds to the negative value, while the solid contours correspond to positive values. Vertical dash–dot lines near the abscissa indicate the edge of the inner layer. Symbols and colours are the same as figure 12.

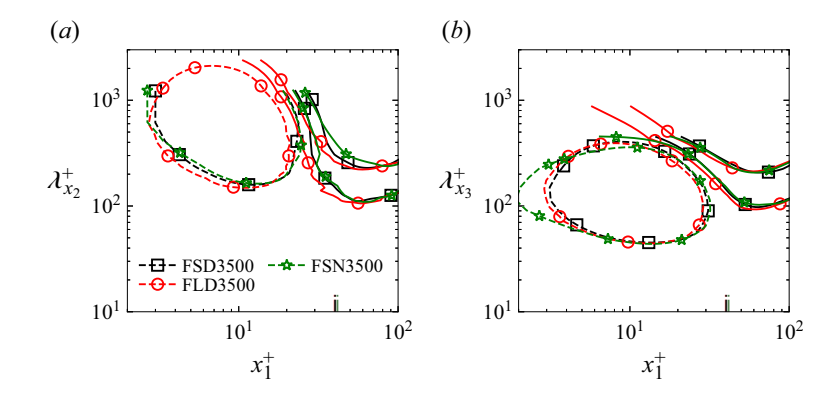


Figure 16. One-dimensional premultiplied cospectra of buoyancy flux $\widehat{P_B^+}$ in the streamwise (a) and spanwise (b) directions at Re = 3500. The contour lines are 0.15 times the minimum of FSD3500 (1.48 × 10⁻³) and 0.15 and 0.45 times the maximum of FSD3500 (1.4 × 10⁻²). The dashed contour corresponds to the negative value, while the solid contours correspond to positive values. Vertical dash–dot lines near the abscissa indicate the edge of the inner layer. Symbols and colours are the same as figure 12.

suggests that the spanwise wavelength of the Q2–Q4 events achieves a fully developed state at moderate Reynolds numbers, unlike the *Re*-dependent streamwise wavelength.

The one-dimensional streamwise and spanwise cospectra of buoyancy flux are shown in figure 16, where it is clear that the wavelengths of positive shear production do not contribute to positive buoyancy flux and that these scales also contribute towards the destruction of TKE (negative buoyancy flux). Similar to what is observed at moderate Reynolds numbers (figure 7), the streamwise and spanwise wavelengths corresponding to negative buoyancy flux approximately coincide with the streamwise and spanwise wavelengths contributing towards positive shear production (which is the induced heat flux discussed in § 3.1). This reiterates that the eddies responsible for shear production in the near-wall region also contribute significantly towards negative buoyancy flux (induced heat flux).

The similarity of the spectra and cospectra of the two different thermal boundary conditions again indicates that there exists an approximate statistical equivalence in the TKE production between the two thermal boundary conditions, similar to what is seen at

https://doi.org/10.1017/jfm.2025.10742 Published online by Cambridge University Press

K.R. Maryada, S.W. Armfield, M. MacDonald, P. Dhopade and S.E. Norris

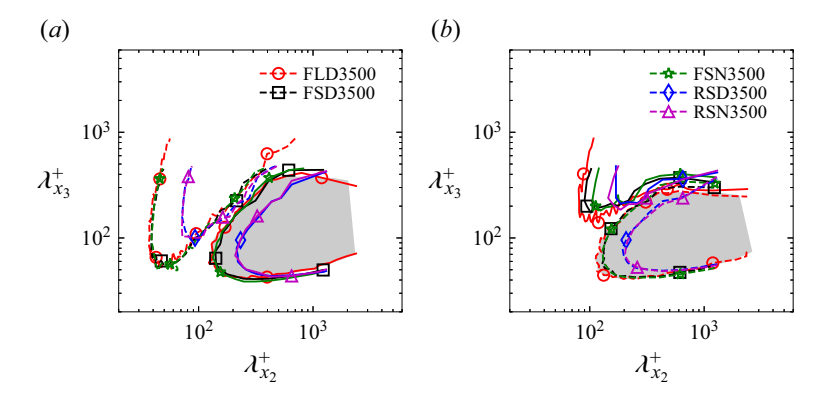


Figure 17. Two-dimensional premultiplied cospectra of (a) shear production $\widehat{P_S^+}$ and (b) buoyant production $\widehat{P_B^+}$ averaged across the inner layer. The contour lines are 0.15 times the minimum $(1.22 \times 10^{-4} \text{ for shear production})$ and 4.77×10^{-4} for buoyant production) and maximum $(2.89 \times 10^{-3} \text{ for shear production})$ and 1.24×10^{-4} for buoyant production) values of RSD3500. Solid contours represent a positive value, while the dashed contour corresponds to a negative value. The grey-shaded region represents positive shear production and negative buoyancy flux of FLD3500. Symbols and colours are the same as figure 12.

moderate Re in § 3.1. Note that at Re = 3500, the Dirichlet and Neumann thermal boundary condition simulations have similar Re_{τ} and Re in that these simulations differ only in terms of thermal boundary conditions.

The shear production and buoyancy flux cospectra in figures 15 and 16 are only marginally different across the different domains and thermal boundary conditions. Figure 17 shows the premultiplied two-dimensional cospectra of shear production and buoyancy flux Re = 3500. The spectral signature of shear production and buoyancy flux of FSD3500 and FSN3500 is similar to FLD3500 (also evident in figures 15 and 16). The contours of positive shear production and negative buoyancy flux of RSD3500 and RSN3500 are in fair agreement with FLD3500 except at $\lambda_{x_2}^+ \approx \lambda_{x_3}^+$, akin to Re = 1400 (figure 10). The peaks of positive shear production and induced heat flux are in very good agreement with each other despite differences observed at $\lambda_{x_2}^+ \approx \lambda_{x_3}^+$.

These findings suggest that despite the wall-normal velocity and buoyancy fluctuations being different, the cross-correlation between u_1 and u_2 , and u_2 and ϑ at the dominant wavelengths of shear production is chiefly independent of the outer layer, LSMs and thermal boundary conditions at moderate and high Re. It is worth pointing out that the near-wall cycle of canonical wall turbulence also does not significantly depend on the distribution of wall-normal velocity fluctuations (Chernyshenko & Baig 2005), akin to what is observed in the present case. Therefore, fundamentally, the near-wall turbulence production of a vertical buoyancy layer at moderate and high Reynolds numbers is similar to the near-wall cycle of canonical wall turbulence. The inner-outer turbulence interaction is not essential to sustaining turbulence but only has a secondary effect, at least in terms of the statistics considered in this study.

We emphasise that the autonomous and self-sustaining nature of the near-wall turbulence in a vertical buoyancy layer does not imply that inner-layer turbulence is entirely independent of the LSMs and bulk flow. The interactions between the inner and outer layers may be present but only marginally influence the low-order statistics such as the spectra and cospectra.

This self-sustaining nature of near-wall turbulence in the absence of LSMs also suggests that the nonlinear energy transfer between different scales in the inner layer of vertical

buoyancy layers is a complex phenomenon much like wall turbulence, and is not merely a transfer from large to small scales at different wall-normal locations and separation vectors (e.g. see Cimarelli *et al.* (2016) and Cho, Hwang & Choi (2018) regarding interscale energy transport in turbulent channels). The detailed interactions between the inner and outer layers and the interscale energy transport in the inner layer have not been investigated further, and examining them is left for future study.

Here, it is worthwhile to mention that the observations presented in this paper are not in agreement with the Grossmann–Lohse theory for vertical convection (Ng et al. 2015, 2017) regarding the idea that the 'turbulent wind' is significant in the sustenance of the ultimate regime (see also Wells & Worster (2008) and Ke et al. (2023)). Despite this, our findings, when taken in context with Ng et al. (2015, 2017) and Ke et al. (2021, 2023), suggest that Grossmann–Lohse theory still provides a valid framework for predicting the scaling of Nusselt number and other mean quantities, even if the 'turbulent wind' does not play the expected role in driving the inner layer in vertical convection. Therefore, future studies on vertical convection should focus on clarifying the exact physical mechanisms responsible for the scaling of the Nusselt number and other bulk quantities.

3.5. A unified picture of near-wall turbulence production in vertical buoyancy layers and canonical wall turbulence

In terms of mean flow and driving mechanisms, it is evident that there is little similarity between vertical buoyancy layers and canonical wall-bounded turbulence. However, from the previous sections, we see that akin to canonical wall-bounded turbulence, the near-wall turbulence, at moderate and high Reynolds numbers, is self-sustaining and largely independent of the outer-layer flow and LSMs.

At both moderate $(800 \le Re \le 2800)$ and high (Re = 3500) Reynolds numbers, irrespective of the thermal boundary condition, the shear production cospectrum exhibits a peak at similar wavelengths (comparing figure 6 with figures 7, 15 and 16), implying that analogous physical processes are responsible for turbulence production in the near-wall region. The sustenance of the near-wall turbulence in buoyancy-driven boundary layer flow, at moderate and high Re, is due to Q2–Q4 Reynolds shear stress events (responsible for positive shear production; see §§ 3.3 and 3.4). Following Jiménez (2022), we term these Q2–Q4 Reynolds shear stress events as 'self-contained bursts'.

The spectral signatures of near-wall streaks are evident at Re = 3500, which are notably absent at $800 \le Re \le 2800$ (comparing figures 4 and 12; also see figure 13). This suggests that inner-layer turbulence production and sustenance do not primarily depend on streaks. As turbulence production in the inner layer occurs at similar wavelengths at both moderate and high Re (without and with near-wall streaks, respectively), it likely implies that the near-wall streaks at Re = 3500 are byproducts and not the essential features of turbulence regeneration in vertical buoyancy layers. These become prominent at high-Re likely due to increased scale separation and mean shear (as discussed in § 3.4).

The above idea of near-wall turbulence is comparable to the self-sustaining process proposed recently by Jiménez (2022), where streaks do not actively contribute to wall turbulence and are viewed as byproducts.

The spanwise wavelength of the self-contained burst attains an approximately constant value of $\lambda_{x_3}^+ \approx 100$ at moderate and high Reynolds numbers (comparing figures 4 and 12), which is consistent with the self-contained burst of canonical wall turbulence. The streamwise wavelength is a function of the Reynolds number (which essentially parametrises the mean shear in the inner layer), with it approaching the value associated with canonical wall turbulence at Re = 3500.

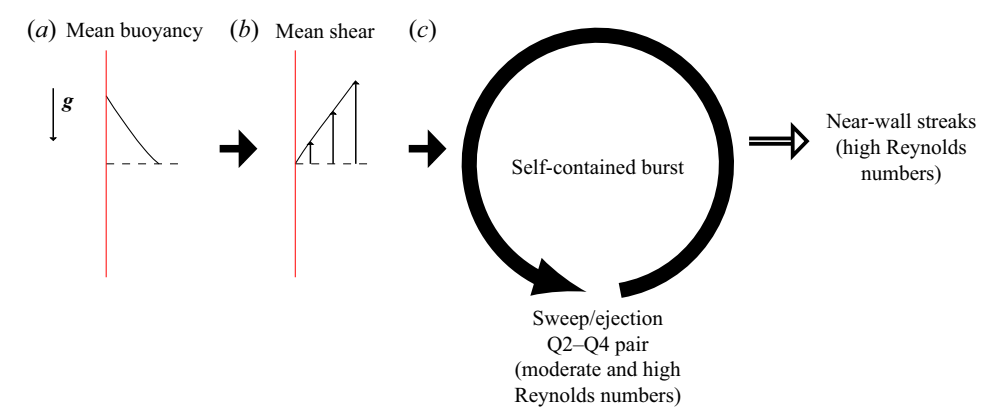


Figure 18. A schematic of the near-wall self-contained burst of vertical buoyancy layers at moderate and high Reynolds numbers. Here, the red vertical line represents the heated wall, and g is the acceleration due to gravity. The solid black horizontal arrows indicate 'cause', depicting a cause-and-effect relationship between the variable in panel (a) and the variable in panel (b). The hollow horizontal arrow indicates that the near-wall streaks are only byproducts at high Re. See text for details.

In §§ 3.3 and 3.4, we have observed that the shear production in the near-wall region is primarily a local process, with its dynamics not significantly depending on the LSMs and the bulk flow. The same is true for canonical wall turbulence, where too the near-wall turbulence is largely independent of the outer-layer turbulence (Jiménez & Moin 1991; Jiménez & Pinelli 1999; Jiménez 2022). The similarity between the self-contained burst of the present buoyancy-driven flow and canonical wall turbulence indicates that the primary role of the buoyancy field is to accelerate the mean flow and not drastically alter the inner layer's turbulent generation mechanism. Therefore, if the terminology commonly used for mixed convection flows is to be employed (e.g. You, Yoo & Choi 2003), at both moderate and high Reynolds numbers, the buoyancy field in a vertical buoyancy layer mainly affects turbulence externally (mean shear) and not structurally (eddy structure). The statistical behaviour of turbulence is mainly governed by shear, which is induced by the mean buoyancy field. If the contrary were true, i.e. buoyancy significantly affects the eddy structure, we would not expect a similarity between the current flow and canonical wall turbulence, which is clearly not the case in the present study.

In terms of causality analysis, one can presume that the mean buoyancy field 'causes' a mean shear, which in turn 'causes' a self-contained burst. This self-contained burst is the fundamental unit of turbulence and is responsible for the inner-layer turbulence sustenance at moderate and high Reynolds numbers. The near-wall streaks only become statistically evident at high Reynolds numbers, which are presumably a byproduct of this self-sustaining process. This process is graphically represented in figure 18.

Finally, we remark that similar conclusions regarding the external effect of the buoyancy field also hold in the outer layer, as the relative scaling of longitudinal structure functions of the vertical buoyancy layer in the outer layer scale similarly to canonical wall turbulence (Maryada *et al.* 2024).

4. Conclusions

This study investigates the inner-layer turbulence of a vertical buoyancy layer (a model for a vertical natural convection boundary layer) at Pr = 0.71 and $200 \le Re \le 3500$ using DNS.

An approximate statistical equivalence exists between the vertical buoyancy layer flow over constant heat flux and constant thermal excess boundary conditions in terms of mean flow and velocity fluctuations. However, this cannot be extended to buoyancy variance and streamwise turbulent heat flux. The mean Reynolds shear stress and the streamwise turbulent heat flux can take either positive or negative values in the inner layer depending on *Re* and thermal boundary conditions. Different physical processes dominate turbulence dynamics as *Re* is varied.

Irrespective of the thermal boundary condition, the inner layer is weakly turbulent at $200 \le Re \le 2800$. It does not exhibit a spectral peak at a spanwise wavelength of 100 viscous units at a wall-normal distance of around 15 viscous units, something that is synonymous with the near-wall (buffer layer) streaks of canonical wall turbulence (canonical wall turbulence). Most of the turbulence is observed in the outer layer in the form of LSMs.

At Re = 200, there is no significant shear production in the near-wall region, with the only production occurring at the edge of the inner layer due to buoyancy. At $800 \le Re \le 2800$, the shear production is positive and turbulence in the inner layer is produced by both shear and buoyancy. Shear production is dominant in the near-wall region, and its spectrum peaks at a spanwise wavelength of 100 viscous units. The thermal boundary condition of the heated wall does not significantly influence the spanwise wavelengths responsible for shear production in the inner layer.

As turbulence is being produced by shear in the inner layer at moderate Reynolds numbers ($800 \le Re \le 2800$), the effect of the outer-layer turbulence and LSMs on inner-layer turbulence is investigated using domains truncated in the streamwise, spanwise and wall-normal directions. We demonstrate that the near-wall turbulence is mainly autonomous and self-sustaining, and the eddies responsible for shear production in the inner layer only marginally depend on the outer-layer turbulence, LSMs and thermal boundary conditions. The interactions between the inner layer turbulence and the LSMs in the outer layer may be present but only marginally influence the low-order statistics, such as the spectra and cospectra.

Based on the observations that the near-wall shear production is autonomous, using minimal domains, the inner-layer turbulence is investigated at a higher Reynolds number to understand the behaviour of the ultimate regime, i.e. a regime where the inner-layer is turbulent in the sense of Prandtl and von Kármán and exhibiting signatures of canonical wall turbulence. For the present case, the critical Reynolds number for transition to the ultimate regime lies in the range $2800 < Re_c < 3500$. At Re = 3500, irrespective of the thermal boundary condition, the buoyancy layer is in the ultimate regime, with the premultiplied energy spectra of streamwise velocity fluctuations exhibiting a distinct peak at a wall-normal location of $x_1^+ \approx 15$ and a spanwise wavelength of $\lambda_{x_3}^+ \approx 100$. The shear production in the near-wall region peaks at a spanwise wavelength of 100 viscous units, akin to what is observed at $800 \le Re \le 2800$.

The inner-layer turbulence production in vertical buoyancy layers is similar at moderate and high Reynolds numbers. It is self-sustaining and primarily autonomous of the outer bulk flow, LSMs and thermal boundary conditions. Near-wall streaks are not essential for this autonomous process. Instead, like canonical wall turbulence (Jiménez 2022), the self-contained burst of Q2–Q4 Reynolds shear stress events is a fundamental unit of turbulence at both moderate and high Reynolds numbers.

On a fundamental level, the near-wall turbulence production of vertical buoyancy layers is predominantly a local process that depends on the mean buoyancy field and not on the bulk flow. The mean buoyancy field primarily sets the level of mean shear, and the

K.R. Maryada, S.W. Armfield, M. MacDonald, P. Dhopade and S.E. Norris

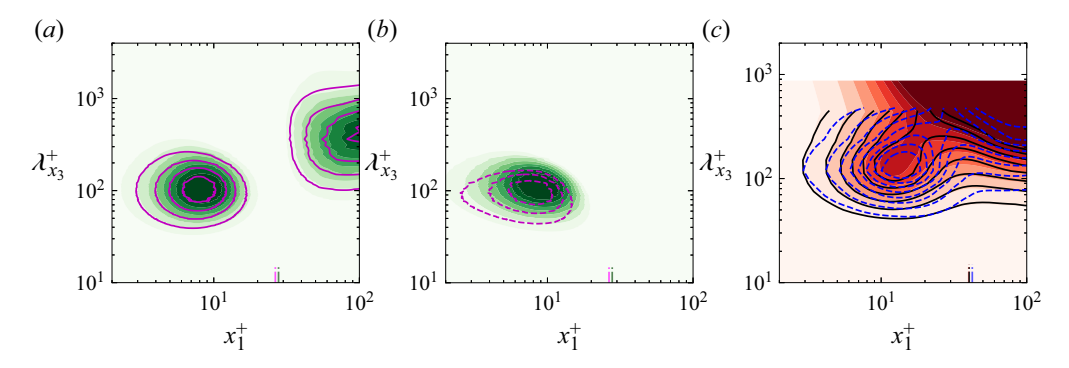


Figure 19. The effect of contour levels on the spectra and cospectra. Panel (a) shows the regions of positive shear production, while panel (b) shows the regions of negative buoyancy flux for FFD1800 (shaded green contours) and FFN2800 (magenta lines) cases. Panel (c) shows the premultiplied energy spectra of streamwise velocity fluctuations in the spanwise direction for FLD3500 (shaded red contours), FSD3500 (solid black lines) and RSD3500 (dashed blue lines). In panel (a), the contours are eight equally spaced levels between 0.1 and 0.8 times the maximum of FFD1800, while in panel (b), these are eight equally spaced levels between 0.1 and 0.8 times the minimum of FFD1800. In panel (c), the contours are eight equally spaced levels between 0.1 and 0.8 times the maximum of RSD3500.

turbulence in the near-wall region is primarily dictated by shear induced by the mean buoyancy field.

Acknowledgements. We thank New Zealand eScience Infrastructure (NeSI) for providing high-performance computational resources.

Funding. This research received no specific grant from any funding agency, commercial or not-for-profit sectors.

Declaration of interests. The authors report no conflict of interest.

Appendix A. Choice of contour levels in the visualisation of spectra and cospectra

Figure 19 shows the premultiplied one-dimensional energy spectra of positive shear production and induced heat flux of FFD1800 and FFN2800, and the premultiplied one-dimensional energy spectra of streamwise velocity fluctuations of FLD3500, FSD3500 and RSD3500. The data is identical to what is seen in figures 6(d), 7(d) and 12(a), but plotted with a higher number of contour levels. At moderate Re, irrespective of the thermal boundary condition, we see positive shear production and negative buoyancy flux in the inner layer at $\lambda_{x_3^+} \approx 100$. At Re = 3500, we see the emergence of a near-wall spectral peak, indicating that the vertical buoyancy layer has transitioned into the ultimate regime. These observations are consistent with the discussion made in § 3, indicating that the same conclusions hold even if different contour levels are used for visualisation. Therefore, changing the number of contour levels does not affect the major conclusions of the current study.

Appendix B. Effect of domain size on Nusselt number

Table 4 shows the effect of domain size on the Nusselt number at Re = 1400. The Nusselt number Nu is defined as (Ke *et al.* 2021, 2023)

$$Nu = \frac{q_w \delta_{bl}}{\rho C_p \alpha \tilde{\vartheta}_w},\tag{B1}$$

Case	Nu
FFD1400	36.83
FSD1400	31.81
RSD1400	10.05
R ₂ SD1400	21.16
RLD1400	10.09

Table 4. The variation of Nusselt number with respect to the domain size at Re = 1400.

where $\tilde{\vartheta}_w$ is the buoyancy field at the heated wall. For FFD1400 and FSD1400, δ_{bl} is defined as the wall-normal location where the mean streamwise velocity changes sign for the first time. For RSD1400, R₂SD1400 and RSD3500, it is defined as the length of the domain in the wall-normal direction. This is done as, in these cases, the wall-normal domain extent is smaller than δ_{bl} .

Despite the near-wall turbulence production being largely autonomous (§ 3.3), we observe that the Nusselt number varies with changing domain size. This indicates that the LSMs and outer layer motions influence the mean Nusselt number and that the wall quantities do not solely depend on the near-wall small scales. This, combined with the results presented in § 3.3 and § 3.4, shows that if one is interested in the turbulence of small scales, minimal domains are sufficient; however, minimal domains are insufficient to understand mean wall quantities such as the Nusselt number.

Appendix C. Mean flow, TKE and buoyancy variance in different domains at Re=3500

The one-dimensional wall-normal profiles of the mean flow, TKE and buoyancy variance are shown in figure 20 to highlight the differences and similarities in the integral statistics. The mean streamwise velocity and buoyancy fields are shown in figures 20(a) and 20(b), and until $x_1^+ \lesssim 10$, there is no noticeable difference between all the cases.

The TKE and buoyancy variance profiles are plotted in figures 20(c) and 20(d). The effects of the domain size and the far-field boundary condition are evident in these figures. Comparing FLD3500 and FSD3500, it is apparent that LSMs make non-negligible contributions to the TKE and buoyancy variance, and hence, changing the domain size changes their magnitude. Due to wall-normal truncation, despite having the same streamwise and spanwise domain sizes, the one-dimensional profiles of RSD3500 and RSN3500 are different from FSD3500 and FSN3500, suggesting that the wall-normal truncation also affects the integral values in both the inner and outer layers. The behaviour of the mean flow and the integral statistics is similar to what is observed at Re = 1400 (see figure 9).

For FSD3500 and FSN3500, and RSD3500 and RSN3500, the mean streamwise velocity and buoyancy fields, and TKE are almost identical, indicating that the exact nature of the thermal boundary condition at the heated wall has very little influence on these quantities. A difference is only observed in the mean temperature variance profiles. This behaviour at high Re in minimal domains is in agreement with what is observed at moderate Re (see § 3.1).

Note that we have matched the Re_{τ} and Re between the two thermal boundary conditions in the ultimate regime; therefore, this set of simulations is a much more stringent test to understand the effect of thermal boundary conditions. We observe the same behaviour as in § 3.1, where there is only an approximate similarity in terms of Re_{τ} . Therefore, this again

K.R. Maryada, S.W. Armfield, M. MacDonald, P. Dhopade and S.E. Norris

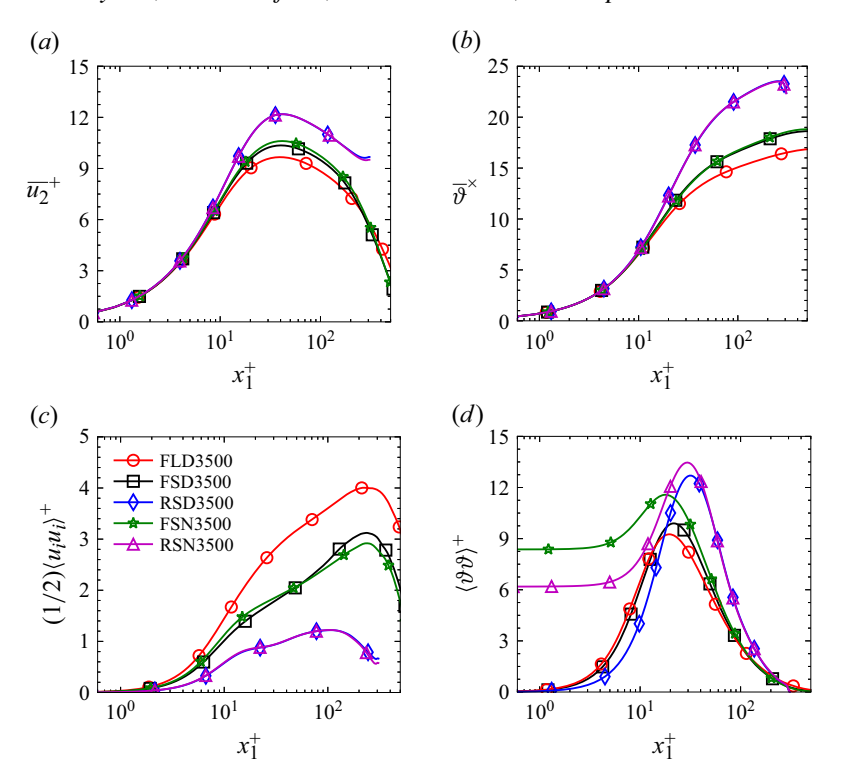


Figure 20. Mean flow and one-point statistics at Re = 3500. Panel (a) corresponds to mean streamwise velocity $\overline{u_2}^+$, panel (b) corresponds to mean temperature field ϑ^\times , panel (c) corresponds to TKE and panel (d) corresponds to buoyancy variance $\langle \vartheta \vartheta \rangle^+$.

confirms that approximate statistical equivalence between vertical convection flows over Dirichlet and Neumann thermal boundary conditions can be considered valid regarding the mean streamwise velocity, buoyancy field and velocity variances, but not in terms of the mean temperature variance.

REFERENCES

ABEDIN, M.Z., TSUJI, T. & HATTORI, Y. 2009 Direct numerical simulation for a time-developing natural-convection boundary layer along a vertical flat plate. *Intl J. Heat Mass Transfer* **52** (19-20), 4525–4534.

DEL Á LAMO, J.C., JIMÉNEZ, J., ZANDONADE, P. & MOSER, R.D. 2004 Scaling of the energy spectra of turbulent channels. *J. Fluid Mech.* **500**, 135–144.

ARMFIELD, S.W. 1991 Finite difference solutions of the Navier–Stokes equations on staggered and non-staggered grids. *Comput. Fluids* **20** (1), 1–17.

ARMFIELD, S.W. 1994 Ellipticity, accuracy, and convergence of the discrete Navier–Stokes equations. J. Comput. Phys. 114 (2), 176–184.

ARMFIELD, S.W., MORGAN, P., NORRIS, S. & STREET, R. 2003 A parallel non-staggered Navier—Stokes solver implemented on a workstation cluster. In *Computational Fluid Dynamics* 2002, pp. 30–45. Springer. BEJAN, A. 2013 *Convection Heat Transfer*, 4th edn. John Wiley & Sons.

CHANDRAN, D., BAIDYA, R., MONTY, J.P. & MARUSIC, I. 2017 Two-dimensional energy spectra in high-Reynolds-number turbulent boundary layers. *J. Fluid Mech.* 826, R1.

CHEESEWRIGHT, R. & DOAN, K.S. 1978 Space-time correlation measurements in a turbulent natural convection boundary layer. *Intl J. Heat Mass Transfer* **21** (7), 911–921.

CHERNYSHENKO, S.I. & BAIG, M.F. 2005 The mechanism of streak formation in near-wall turbulence. *J. Fluid Mech.* **544**, 99–131.

CHO, M., HWANG, Y. & CHOI, H. 2018 Scale interactions and spectral energy transfer in turbulent channel flow. J. Fluid Mech. 854, 474–504.

- CIMARELLI, A., DE ANGELIS, E., JIMÉNEZ, J. & CASCIOLA, C.M. 2016 Cascades and wall-normal fluxes in turbulent channel flows. *J. Fluid Mech.* **796**, 417–436.
- COSSU, C. & HWANG, Y. 2017 Self-sustaining processes at all scales in wall-bounded turbulent shear flows. Phil. Trans. R. Soc. Lond. A 375 (2089), 20160088.
- DESHPANDE, R., MONTY, J.P. & MARUSIC, I. 2021 Active and inactive components of the streamwise velocity in wall-bounded turbulence. *J. Fluid Mech.* 914, A5.
- FAN, Y., ZHAO, Y., TORRES, J.F., XU, F., LEI, C., LI, Y. & CARMELIET, J. 2021 Natural convection over vertical and horizontal heated flat surfaces: a review of recent progress focusing on underpinnings and implications for heat transfer and environmental applications. *Phys. Fluids* 33 (10), 101301.
- FEDOROVICH, E. & SHAPIRO, A. 2009 Turbulent natural convection along a vertical plate immersed in a stably stratified fluid. *J. Fluid Mech.* **636**, 41–57.
- FLORES, O. & JIMÉNEZ, J. 2010 Hierarchy of minimal flow units in the logarithmic layer. *Phys. Fluids* **22** (7), 071704.
- GAYEN, B., GRIFFITHS, R.W. & KERR, R.C. 2016 Simulation of convection at a vertical ice face dissolving into saline water. J. Fluid Mech. 798, 284–298.
- GILL, A.E. 1966 The boundary-layer regime for convection in a rectangular cavity. *J. Fluid Mech.* **26** (3), 515–536.
- GILL, A.E. & DAVEY, A. 1969 Instabilities of a buoyancy-driven system. J. Fluid Mech. 35 (4), 775–798.
- GIOMETTO, M.G., KATUL, G.G., FANG, J. & PARLANGE, M.B. 2017 Direct numerical simulation of turbulent slope flows up to Grashof number $Gr = 2.1 \times 10^{11}$. J. Fluid Mech. 829, 589–620.
- GROSSMANN, S. & LOHSE, D. 2000 Scaling in thermal convection: a unifying theory. J. Fluid Mech. 407, 27–56
- HATTORI, Y., TSUJI, T., NAGANO, Y. & TANAKA, N. 2006 Turbulence characteristics of natural-convection boundary layer in air along a vertical plate heated at high temperatures. *Intl J. Heat Fluid Flow* 27 (3), 445–455.
- HOWLAND, C.J., NG, C.S., VERZICCO, R. & LOHSE, D. 2022 Boundary layers in turbulent vertical convection at high Prandtl number. J. Fluid Mech. 930, A32.
- HUTCHINS, N. & MARUSIC, I. 2007 Large-scale influences in near-wall turbulence. Phil. Trans. R. Soc. Lond. A 365 (1852), 647–664.
- HWANG, J., LEE, J.H. & SUNG, H.J. 2020 Statistical behaviour of self-similar structures in canonical wall turbulence. J. Fluid Mech. 905, A6.
- HWANG, Y. 2013 Near-wall turbulent fluctuations in the absence of wide outer motions. J. Fluid Mech. 723, 264–288.
- HWANG, Y. 2015 Statistical structure of self-sustaining attached eddies in turbulent channel flow. J. Fluid Mech. 767, 254–289.
- JIMÉNEZ, J. 2022 The streaks of wall-bounded turbulence need not be long. J. Fluid Mech. 945, R3.
- JIMÉNEZ, J., DEL ALAMO, J.C. & FLORES, O. 2004 The large-scale dynamics of near-wall turbulence. J. Fluid Mech. 505, 179–199.
- JIMÉNEZ, J. & MOIN, P. 1991 The minimal flow unit in near-wall turbulence. J. Fluid Mech. 225, 213-240.
- JIMÉNEZ, J. & PINELLI, A. 1999 The autonomous cycle of near-wall turbulence. J. Fluid Mech. 389, 335–359.
- KE, J., WILLIAMSON, N., ARMFIELD, S.W. & KOMIYA, A. 2023 The turbulence development of a vertical natural convection boundary layer. *J. Fluid Mech.* **964**, A24.
- KE, J., WILLIAMSON, N., ARMFIELD, S.W., KOMIYA, A. & NORRIS, S.E. 2021 High Grashof number turbulent natural convection on an infinite vertical wall. *J. Fluid Mech.* **929**, A15.
- KE, J., WILLIAMSON, N., ARMFIELD, S.W., NORRIS, S.E. & KOMIYA, A. 2020 Law of the wall for a temporally evolving vertical natural convection boundary layer. *J. Fluid Mech.* **902**, A31.
- KIŠ, P. & HERWIG, H. 2012 The near wall physics and wall functions for turbulent natural convection. *Intl J. Heat Mass Transfer* **55** (9–10), 2625–2635.
- KLINE, S.J., REYNOLDS, W.C., SCHRAUB, F.A. & RUNSTADLER, P.W. 1967 The structure of turbulent boundary layers. *J. Fluid Mech.* **30** (4), 741–773.
- KOZUL, M., CHUNG, D. & MONTY, J.P. 2016 Direct numerical simulation of the incompressible temporally developing turbulent boundary layer. *J. Fluid Mech.* **796**, 437–472.
- KRAICHNAN, R.H. 1962 Turbulent thermal convection at arbitrary Prandtl number. *Phys. Fluids* 5 (11), 1374–1389.
- LEE, M. & MOSER, R.D. 2015 Direct numerical simulation of turbulent channel flow up to $Re_{\tau} \approx 5200$. J. Fluid Mech. 774, 395–415.
- LEE, M. & MOSER, R.D. 2019 Spectral analysis of the budget equation in turbulent channel flows at high Reynolds number. *J. Fluid Mech.* **860**, 886–938.
- LEE, M.J., KIM, J. & MOIN, P. 1990 Structure of turbulence at high shear rate. J. Fluid Mech. 216, 561-583.

K.R. Maryada, S.W. Armfield, M. MacDonald, P. Dhopade and S.E. Norris

- LIN, W. & ARMFIELD, S.W. 2005 Unsteady natural convection on an evenly heated vertical plate for Prandtl number Pr < 1. Phys. Rev. E 72 (6), 066309.
- LIN, W., ARMFIELD, S.W. & PATTERSON, J.C. 2008 Unsteady natural convection boundary-layer flow of a linearly-stratified fluid with Pr < 1 on an evenly heated semi-infinite vertical plate. *Intl J. Heat Mass Transfer* **51** (1–2), 327–343.
- LOZANO-DURÁN, A. & BAE, H.J. 2019 Characteristic scales of Townsend's wall-attached eddies. J. Fluid Mech. 868, 698–725.
- MACDONALD, M., CHUNG, D., HUTCHINS, N., CHAN, L., OOI, A. & GARCÍA-MAYORAL, R. 2017 The minimal-span channel for rough-wall turbulent flows. *J. Fluid Mech.* **816**, 5–42.
- MARYADA, K.R., ARMFIELD, S.W., DHOPADE, P. & NORRIS, S.E. 2022 Oblique-mode breakdown of the vertical buoyancy layer. *J. Fluid Mech.* **953**, A34.
- MARYADA, K.R., ARMFIELD, S.W., DHOPADE, P. & NORRIS, S.E. 2023 Large-scale motions in a turbulent natural convection boundary layer immersed in a stably stratified environment. *J. Fluid Mech.* **967**, A40.
- MARYADA, K.R., ARMFIELD, S.W., MACDONALD, M., DHOPADE, P. & NORRIS, S.E. 2024 Universal relative scaling of longitudinal structure functions in shear-dominated turbulence. *J. Fluid Mech.* **984**, A28.
- MCBAIN, G.D., ARMFIELD, S.W. & DESRAYAUD, G. 2007 Instability of the buoyancy layer on an evenly heated vertical wall. *J. Fluid Mech.* **587**, 453–469.
- MCCONNOCHIE, C.D. & KERR, R.C. 2016 The turbulent wall plume from a vertically distributed source of buoyancy. *J. Fluid Mech.* **787**, 237–253.
- MIYAMOTO, M. & OKAYAMA, M. 1982 An experimental study of turbulent free convection boundary layer in air along a vertical plate using LDV. *Bull. JSME* **25** (209), 1729–1736.
- MOIN, P. & KIM, J. 1982 Numerical investigation of turbulent channel flow. J. Fluid Mech. 118, 341–377.
- NAKAO, K., HATTORI, Y. & SUTO, H. 2017 Numerical investigation of a spatially developing turbulent natural convection boundary layer along a vertical heated plate. *Intl J. Heat Fluid Flow* **63**, 128–138.
- NAKAO, K., HATTORI, Y., SUTO, H., TAKIMOTO, H. & NIIDA, Y. 2023 Scaling high Rayleigh number natural convection boundary layer statistics: a vertical water tunnel experiment. *Phys. Fluids* **35** (11), 115130.
- NG, C.S., OOI, A., LOHSE, D. & CHUNG, D. 2015 Vertical natural convection: application of the unifying theory of thermal convection. *J. Fluid Mech.* **764**, 349–361.
- NG, C.S., OOI, A., LOHSE, D. & CHUNG, D. 2017 Changes in the boundary-layer structure at the edge of the ultimate regime in vertical natural convection. *J. Fluid Mech.* **825**, 550–572.
- NORRIS, S.E. 2000 A parallel Navier–Stokes solver for natural convection and free surface flow. PhD thesis, The University of Sydney, Camperdown, Sydney.
- PARKER, D.A., BURRIDGE, H.C., PARTRIDGE, J.L. & LINDEN, P.F. 2021 Vertically distributed wall sources of buoyancy. Part 1. Unconfined. *J. Fluid Mech.* 907, A15.
- PATANKAR, S.V. 1980 Numerical Heat Transfer and Fluid Flow. Taylor & Francis.
- PRANDTL, L. 1952 Essentials of Fluid Dynamics. Blackie & Son.
- RHIE, C.M. & CHOW, W.-L. 1983 Numerical study of the turbulent flow past an airfoil with trailing edge separation. *AIAA J.* 21 (11), 1525–1532.
- SCHUMANN, U. 1990 Large-eddy simulation of the up-slope boundary layer. Q. J. R. Meteorol. Soc. 116 (493), 637–670.
- SEBILLEAU, F., ISSA, R., LARDEAU, S. & WALKER, S.P. 2018 Direct numerical simulation of an air-filled differentially heated square cavity with Rayleigh numbers up to 10¹¹. *Intl J. Heat Mass Transfer* 123, 297–319.
- SHAPIRO, A. & FEDOROVICH, E. 2004 Unsteady convectively driven flow along a vertical plate immersed in a stably stratified fluid. *J. Fluid Mech.* **498**, 333–352.
- TAO, J., LE QUÉRÉ, P. & XIN, S. 2004 Spatio-temporal instability of the natural-convection boundary layer in thermally stratified medium. J. Fluid Mech. 518, 363–379.
- TENNEKES, H. & LUMLEY, J.L. 1972 A First Course in Turbulence. MIT press.
- To, W.M. & HUMPHREY, J.A.C. 1986 Numerical simulation of buoyant, turbulent flow—I. Free convection along a heated, vertical, flat plate. *Intl J. Heat Mass Transfer* 29 (4), 573–592.
- TSUJI, T. & NAGANO, Y. 1988a Characteristics of a turbulent natural convection boundary layer along a vertical flat plate. *Intl J. Heat Mass Transfer* **31** (8), 1723–1734.
- TSUJI, T. & NAGANO, Y. 1988b Turbulence measurements in a natural convection boundary layer along a vertical flat plate. *Intl J. Heat Mass Transfer* **31** (10), 2101–2111.
- VLIET, G.C. & LIU, C.K. 1969 An experimental study of turbulent natural convection boundary layers. J. Heat Transfer 91 (4), 517–531.
- WALLACE, J.M. 2016 Quadrant analysis in turbulence research: history and evolution. *Annu. Rev. Fluid Mech.* 48, 131–158.

- Wells, A.J. & Worster, M.G. 2008 A geophysical-scale model of vertical natural convection boundary layers. *J. Fluid Mech.* **609**, 111–137.
- YIN, G., HUANG, W.-X. & XU, C.-X. 2018 Prediction of near-wall turbulence using minimal flow unit. J. Fluid Mech. 841, 654-673.
- YOU, J., YOO, J.Y. & CHOI, H. 2003 Direct numerical simulation of heated vertical air flows in fully developed turbulent mixed convection. *Intl J. Heat Mass Transfer* 46 (9), 1613–1627.
- ZHAO, Y., LEI, C. & PATTERSON, J.C. 2017 The K-type and H-type transitions of natural convection boundary layers. *J. Fluid Mech.* **824**, 352–387.